FIRE RESISTANCE OF COMPOSITE SLABS WITH STEEL DECK AND INSULATION MATERIAL

Gabriel Turczyn De Lucca - a57032

Dissertation presented to the School of Technology and Management of Bragança to obtain the Master's Degree in Engenharia da Construção.

Work oriented by:
Prof. Paulo Alexandre Gonçalves Piloto
Prof. Carlos Balsa
Prof. Erica Kimura

Bragança
2023/2024

INSTITUTO POLITÉCNICO DE BRAGANÇA
Escola Superior de Tecnologia e Gestão

UNIVERSIDADE TECNOLÓGICA FEDERAL DO PARANÁ
CAMPUS CURITIBA

FIRE RESISTANCE OF COMPOSITE SLABS WITH STEEL DECK AND INSULATION MATERIAL

Gabriel Turczyn De Lucca - a57032

Dissertation presented to the School of Technology and Management of Bragança to obtain the Master's Degree in Engenharia da Construção within the double degree program between IPB and UTFPR.

Work oriented by:
Prof. Paulo Alexandre Gonçalves Piloto
Prof. Carlos Balsa
Prof. Erica Kimura

Bragança
2023/2024

Acknowledgement

First and foremost, I would like to express my profound gratitude to my family: my father, Antonio, my mother, Sheila, and my sister, Duda. Your support and encouragement were crucial throughout my dual-degree journey. Without your support, none of this would have been possible. I am thankful to my partner, Laura, who stood by my side, offering support and understanding throughout the entire dual-degree process. Her presence was essential in keeping me motivated and focused.

I extend my gratitude to my advisors at IPB, Professor Dr. Paulo Alexandre Piloto and Professor Dr. Carlos Balsa. Your expertise and dedication were crucial in shaping my knowledge and in the development of this dissertation. I also thank Professor Dr. Erica Kimura from UTFPR for her support and the countless hours dedicated, contributing to the completion of this work.

I also want to extend my thanks to all the friends who were by my side during this exchange period. The friendships formed are true treasures that I will carry for life, making this academic experience even more enriching and meaningful.

Finally, I am grateful to the institutions Instituto Politécnico de Bragança (IPB) and Universidade Tecnológica Federal do Paraná (UTFPR) for providing me with this dual-degree opportunity and for supplying all the necessary support for the realization and completion of this dissertation.

Abstract

A composite slab is defined as a steel profile with concrete on top, and when the concrete reaches its expected strength, the two elements start to work as one through indentations and geometry. This technology has been used since the 1980s in Europe, mainly in the United Kingdom; however, it was only in 1983 that the first technical standard for the calculation of this type of structure was released.

These standards were and still are based on experimental studies by various authors. However, since the cost of conducting these tests is very high, the technique of using finite elements and numerical simulation has been expanding in recent years as an alternative to replace or validate these laboratory studies, proving to be highly effective when properties are correctly inserted.

This dissertation presents the numerical study conducted to validate the temperature field of a laboratory experiment, using the ANSYS software. It also validates the maximum load-bearing capacity at ambient temperature compared to analytical calculation and presents the calculation of the maximum load-bearing capacity when the temperature field is applied for up to 120 minutes.

The study proved capable of representing temperature fields and validating the load-bearing capacity of the slab in the software, demonstrating that such studies when the correct properties are applied, can support experimental studies.

Keywords: Composite slab; Finite elements; Numerical simulation; Fire resistance

Resumo

Laje mista é definida como um perfil de aço com concreto no topo, e quando o concreto atinge sua resistência esperada, os dois elementos passam a trabalhar como um só por meio de reentrâncias e geometria. Essa tecnologia vem sendo utilizada desde os anos de 1980 na Europa, principalmente no Reino Unido; porém, apenas no ano de 1983 foi lançada a primeira normativa técnica para o cálculo deste tipo de estrutura.

Tais normativas se baseavam e ainda se baseiam em estudos experimentais de diversos autores, porém, como o custo de elaboração destes testes é muito elevado, a técnica do uso de elementos finitos e simulação numérica vem se expandindo nos últimos anos, como uma alternativa para substituir ou validar esses estudos em laboratório, provando-se altamente eficaz quando as propriedades são inseridas de forma correta.

Esta dissertação apresenta o estudo numérico realizado para a validação do campo de temperaturas de um experimento em laboratório por meio do software ANSYS, a validação da capacidade portante máxima à temperatura ambiente comparada ao cálculo analítico, e a apresentação do cálculo da capacidade portante máxima quando aplicado o campo de temperaturas até 120 minutos.

O estudo provou-se capaz de representar os campos de temperatura e validar a capacidade resistente da laje no software, mostrando que tais estudos, quando aplicadas as propriedades corretas, podem servir de ajuda aos estudos experimentais.

Palavras chave: Laje mista; Elementos finitos; Simulação numérica; Resistência ao fogo

Contents

List of Tables

List of Figures

Chapter 1

Introduction

No money is received from an investment in construction until it is completed and, a factor that greatly influences this statement is the time spent on building a typical floor. Looking for answers to speed up the time of construction, the composite slab can be advantageous over traditional concrete slabs made in situ [1]. The use of composite slabs as a form of construction began in the United States and gained popularity in Europe and the rest of the world.

Composite slabs are defined as profiled steel decking with concrete on top, where the deck functions as permanent formwork. When the concrete reaches its full strength, the steel and concrete collaborate as a unified structural element [2]. No other materials give a better combination than steel-concrete when considering that concrete has low cost, high strength, high corrosion resistance, abrasion resistance, and fire resistance, giving the steel protection during an event of fire [1].

Safety against fire is a crucial factor when choosing the type of structure, traditional concrete slabs can be more effective in the event of fire due to the concrete being able to provide protection to the steel and delay the drop in resistance [1].

Due to a lack of research in the field of fire events, the use of composite slabs in the United

Kingdom was delayed and only gained a significant increase after the 1980s, following research findings that demonstrated the ability of composite slabs to withstand 90 minutes of fire. Despite the high costs associated with such research, they represented only a fraction of the sales and project potential realized with these slabs [3].

This technology can reduce the self-weight of the structure and, as a result, reduce the forces in those components supporting them, such as foundations and columns. The construction speed is significantly affected by its ability to support its weight and work as a complete slab without the need for curing time, on tall buildings the decks can be lifted in large packages and separated on the floor area, which is an advantage compared to the traditional model. The composite slab gains increased appeal due to the growing demand to expand column spacing [4].

As the cost of construction consistently increases due to various factors, the implementation of composite slabs can reduce labor costs, given that this system eliminates the necessity of removing temporary formwork. The outer job is also cleaner and more accessible to the workers, materials, and deliveries. The pre-engineered raceways for electrification and communication from various manufacturers are economically efficient for clients [5].

Given the relativity light weight of the steel deck due to its thickness and the fact that most of the decks already come pre-cut, the transportation is facilitated [2].

One of the most important aspects of designing a building is the thermal comfort that the designer has to provide for its users. This thermal comfort can be defined as the amount of heat the building is going to gain or lose, according to the outside temperature [6]. In the past years, various materials have been used to control this temperature. Taking the safety of the building into consideration, these thermal insulation materials can be used also as fire protection materials, to avoid or delay the collapse of the structure.

Concrete can be considered as a form of passive protection against fire due to its thermal properties. Normal weight concrete has between 1,5 and 3% of water in its composition that, in the event of a fire, this water will evaporate because of the heat and absorb a great amount of heat, delaying the temperature increase at the fire site. Another noteworthy fire protection attribute is the inherent non-combustibility of concrete [7].

When using the steel-deck system as a form of structure, tempering of the steel is a major challenge, since the material will be exposed and will not have the traditional concrete to protect its properties. To solve this issue, adding a layer of zinc (Zn) can be a solution, given the zinc will act as a cathode in the metal corrosion reaction [8].

1.1 State of art

Even though composite slabs had already been used in Europe, the first recommendation for the calculation of the fire resistance of composite slabs was introduced by the European Convention for Constructional Steelwork (ECCS) in 1983 [9]. This guideline was used to base the elaboration of the section on composite slabs in Eurocode 4 Part 1.2. [10], which introduced a simple method of calculating the fire resistance based on the ISO 834 [11] curve. The minimum requirement of fire protection needed for composite slabs was 30 minutes of required fire resistance time, and, to achieve this, no additional calculation needed to be done. To increase the fire resistance from 30 minutes to 60 minutes, additional measures such as reinforcements and insulating coats were necessary [12]. As the heat is transferred from the bottom of the slab to the top, the use of a positive reinforcement in the middle and a negative reinforcement up on the top can increase the structural resistance during the fire, since the increase of the temperature on the positive reinforcement is less rapidly than the bottom and the negative reinforcement is relatively slow.

Later between 1983 and 1985, the main manufacturer of steel decks in the UK commissioned an experimental test conducted by the Construction Industry Research & Information Association (CIRIA), to demonstrate that continuous composite slabs, incorporating standard mesh reinforcement, could achieve fire resistance of 90 minutes [3].

While the CIRIA tests were happening, between 1984 and 1986 the British Steel Corporation (BSC), supported by the Fire Research Station (FRS) and the Department of Environment, conducted an experimental test that had the objective of demonstrating the viability of the fire engineering method in determining fire behavior of composite slabs, by carrying out large-scale fire tests with spans of 7.0 meters. All 3 tests conducted by FRS exceeded 90 minutes of fire resistance. The moisture of the normal-weight concrete (NWC) was 3.3% indicating a normal level of moisture, that couldn't interfere significantly with the test results [3].

One of the most significant full-scale tests conducted on composite steel structures in fire conditions was carried out by the Building Research Establishment (BRE) in Cardington, UK 1990. The results of this test demonstrated that the composite floor structure could withstand significantly higher levels of flexural load than originally anticipated.

Given that any experiment in the laboratory costs a considerable amount of money, the development of thermal and mechanical numerical models to simulate the real conditions of the slabs became an important strategy for analyzing such behavior. In 1991 Hamerlinck described the behavior of a fire-exposed composite steel/concrete slab by comprising a thermal submodel and a mechanic submodel. These models were validated by an experimental test performed at the Centre for Fire Research TNO Building and Construction Research in 1989 sponsored by the European Coal and Steel Community (ECSC) [13].

In 1995, Hammerlinck et al. [12] published an article reviewing the Eurocode 1994 Part 1.2 [14]. They asserted that the EC calculation method was excessively conservative, attributing this to a scarcity of test information. The calculation method considered the temperature distribution relied on conventional rules rather than heat-flow calculations, the load-bearing capacity was determined using the elementary theory of plasticity, and the influence of steel sheet on the load-bearing capacity at elevated temperatures was overlooked.

The heat-flow distribution on a composite slab under fire is essentially two-dimensional due to its profiled deck. The different and non-linear properties of steel and concrete contribute to creating a void, called an air gap, between the concrete and the steel as the temperature increases, after this stage the structure ceases to work as a composite structure. In 1996 these new parameters were implanted in the finite element program DIANA and a numerical simulation was developed to describe the two and three-dimensional heat flow in fire-exposed composite slabs, presenting a good agreement with test results [15]

In 1999, a steel-framed test building was constructed to simulate a standard modern city center eight-story office development, with sandbags representing the load. When applying a fire test in the building, it was identified that the structure did not collapse even though the unprotected beams reached temperatures over 900°C, and, as was expected, the existing fire design codes are too conservative [16]. Leading these discoveries, in 2000, a new method of calculating the steel was proposed [17].

Concerning the behavior of structures submitted to thermal and mechanical load, the numerical modeling approach is an important resource for understanding different types of collapse modes. Once it is accurately carried out, numerical modeling can substitute the necessity of a huge amount of specimens in experimental analysis [18]. Noteworthy finite element programs include ANSYS, ABAQUS, SAFIR (2000), and TASEF (1990).

FEM has been widely used for thermal and mechanical analysis of structural elements, including composite slab elements. An example is the model proposed by Piloto et al [19] for evaluating critical temperature in trapezoidal composite slabs. This model investigated thermal and mechanical behavior considering variations in slab thickness, using the ANSYS software.

With an increase in the detail of materials available in finite element software, it has become possible to expand and enhance the study of new possibilities. This allows for a more detailed representation of phenomena occurring in laboratory experiments or real-scale events. In this context, in 2019, Balsa et al [20] developed numerical methods using ANSYS software to implement an air gap between the contact surface of the steel deck and the concrete. This event occurs when such surfaces are affected by fires. Such enhancement is possible with the implementation of shell elements in the software, where a single element can have one or more layers with different thicknesses and physical properties.

The standard calculation methods for composite slabs are based on real-scale experiments, numerical methods, and analytical methods. The numerical and analytical methods are calibrated according to experimental data, a recent real-scale experiment was conducted by Bolina in 2019 [21]. It revealed that approximately 5 minutes after exposing the slab to the ISO 834 fire curve, there was a detachment between the contact surface of the steel deck and the concrete. This demonstrates that for most of the slab's exposure to fire, the element does not work as a composite structure.

In 2021, Balsa et al. [22] developed a computational model to simulate the thermal behavior of composite slabs under standard fire conditions. Through parametric analysis, they determined temperatures for various composite slab geometries. The model they proposed captured effects that the current Eurocode overlooks, such as the debonding effect between the steel deck and concrete and the thickness of the concrete topping. The new calculation method they introduced incorporates an additional term into the existing formulation, accounting for the thickness of the concrete topping.

In 2023, Bolina [23] conducted experiments testing two scenarios of composite slabs under fire conditions. One scenario applied a constant temperature field with a variable load, while the other applied a temperature based on ISO 834 for up to 180 minutes with a constant load. It was demonstrated that the current standard calculation method is based on the constant temperature and variable load, scenario one, thus not capturing the increase in structural stress levels during temperature rise. However, according to the author, the constant load and variable temperature scenario can represent more realistic situations.

Piloto et al. (2024) [24] conducted numerical studies using finite element software to validate the temperature field in a commercial composite slab. The study demonstrated the effectiveness of correctly implementing convergence factors as well as the boundary conditions of the element. The airgap created between the concrete and the steel deck was modeled using shell elements with multiple layers and different properties for the air and steel.

The numerical modeling proposed in this thesis involves defining the thermal and mechanical properties of the materials used, as well as the numerical method applied in calculating the temperature fields of materials, state of stress, deformations, and displacements. The most commonly used programs, such as ANSYS, use FEM to process the solution of this and many other physical problems of continuous media.

In the context of thermal analyses, the two-dimensional model demonstrates greater accuracy by conducting only a cross-sectional analysis and allowing the verification of temperature gradients in the relevant section [25]. Regarding to mechanical behavior of structural members, such as beams and slabs, at ambient or elevated temperature, the distribution of stress and strain, as well as the displacement along their span, are spacial, so a 3D volumetric model is requested.

1.2 Research objectives

The search for new ways to enhance fire safety in structures has been presenting new possibilities. With the rising popularity of suspended ceiling systems, the adoption of a composite slab system has become increasingly viable, offering the advantage of concealing the structure.

Over time, the steel and composite construction industry has introduced innovative solutions in composite slabs. In this scenario, researching to investigate their efficiency, especially when subjected to high temperatures, is important.

The main objective of this thesis was to perform a numerical simulation using the finite element method to analyze a fire scenario in a composite slab made of steel and concrete, filled with a thermal blanket. The simulation is based on a full-scale experiment specifically focused on fire [26]. The approach outlined aimed not only to replicate the thermal effects exerted by the fire on the slab but also to model the behavior of the structure under the application of a load, with the goal of simulating conditions that resemble reality.

The overall objective is divided into the following specific objectives:

- Develop a numerical model using the non linear thermal properties and determine the temperature field in materials resulting from applied thermal action.
- Develop a numerical model representing the mechanical properties, which vary with the temperature of the materials, as well as the applied actions, and consequently, the behavior of the material analyzed through its stress, strain, and displacement fields.
- Validate the numerical models by comparing them with experimental results already conducted and published in the literature.
- Determine the resistance of the composite slab subjected to high temperatures based on criteria established by normative codes, namely, insulation, integrity, and mechanical strength.

The composite structure studied in this thesis comprises a steel deck, functioning as a permanent formwork, along with mineral wool employed to delay the impact of fire on the slab, thereby ensuring prolonged structural safety. This assembly includes two 10 mm-diameter reinforcement bars known as 'refont au feu' for fire protection, a 5.5mm diameter steel mesh to prevent concrete cracking during a fire, and a concrete layer designed to withstand compression forces and meet the requisite criteria for slab protection.

The slab modeled in the ANSYS software, as illustrated in Figure 1.1 consists of a galvanized steel sheet with a thickness of 1mm, mineral wool with a density of 50 kg/m^3, concrete to withstand compressive forces, and $10mm$ and $5.5mm$ steel bars to support positive and negative bending forces, respectively. Figure 1.2 shows the slab used in the laboratory study. There is also the possibility to add an extra thermal protection to the bottom of the steel deck, as represented in Figure 1.2. Figure 1.3 shows the representation of the COFRADAL 200 slab and its components.

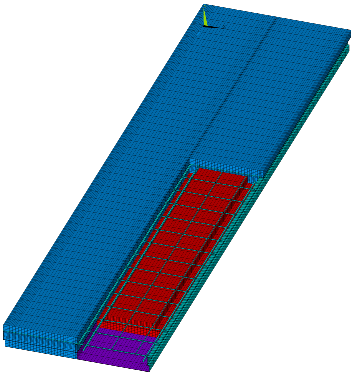

Figure 1.1: Model of the slab (ANSYS)

Figure 1.2: ArcelorMittal Slab

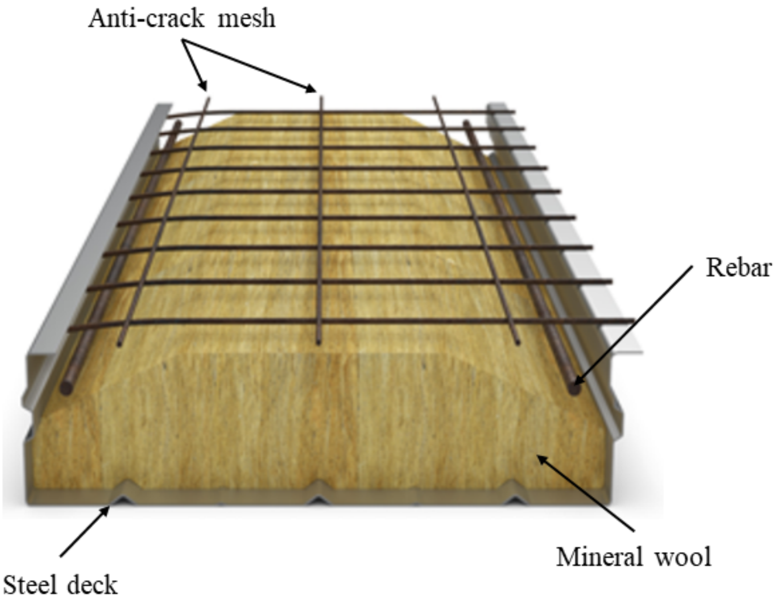

Figure 1.3: COFRADAL 200 - ArcelorMittal

Chapter 2

Heat transfer and material properties

2.1 Heat Transfer

Çengel [27] defines heat as a form of energy that can be transferred from one body to another, and that happens because of the difference in temperature between those bodies. These changes are going to happen always from the high-temperature body to the lower-temperature body and will happen in three different modes, such as, conduction, convection, and radiation.

2.1.1 Conduction

Conduction is a form of energy transfer between the most energy-loaded substance or body to the least energy-loaded substance or body. This transfer can happen between solids, gases, and liquids. In liquids and gases, this conduction happens because of collisions and diffusion of the molecules during a random movement; in solids, it happens according to the vibration rate and free electrons transfer it. The transfer rate will depend on the geometry, thickness, and material of the substance or body [27].

The French Mathematician Fourier [28] described conductivity as a transfer of heat from a hot body to a cold body, tending to lower the temperature of the hot body and increase the temperature of the cold body. The representation of this phenomenon can be found using the Equation 2.1 below.

$$Q = -\lambda \frac{dT}{dx} \tag{2.1}$$

Where Q is the heat flux (W/m^2), λ is the Thermal Conductivity, dT is the difference between the temperature of the materials and dx is the distance in which the heat flows by the contact area.

2.1.2 Convection

Çengel [27] describes convection as a way of transferring energy between a solid surface and the adjacent liquid or gas that is in motion. The fluid motion and the convection heat transfer are proportional, the faster the fluid, the greater the convection. The heat transfer that occurs by convection is ruled by the Newton's law of cooling, as described by the Equation 2.2 below.

$$q = \overline{h} A (T_\infty - T_s) \tag{2.2}$$

Where q is the heat flow (W/m^2), $\overline{h}$ is the average coefficient of heat transfer by convection, A is the area of the surface where the heat transfer occurs, T_∞ is the fluid temperature far from the surface and T_s is the surface temperature.

2.1.3 Radiation

Unlike conduction and convection, radiation is a form of transferring heat that happens through electromagnetic waves (or photons) and does not need the presence of an intervening medium. Radiation is the fastest means of heat transfer, moving at the speed of light, and does not lose or suffer attenuation in a vacuum [27]. The maximum amount of radiation a body can emit is called a blackbody radiation. This name implies that these bodies are black in the sense that they absorb all visible light and other types of radiation that reach them [29]. However, the radiation emitted by all real surfaces is less than that of a blackbody. This radiation can be defined by the Stefan-Boltzmann law.

The factor that distinguishes radiation from a blackbody to real surfaces is emissivity, the value of this parameter ranges between 0 and 1 and measures how close the surface approximates a blackbody, which $\varepsilon = 1$. The Stefan-Boltzmann law to calculate the radiation heat flow (W/m^2) is given by the Equation 2.3 below.

$$\dot{Q}_{emit} = \varepsilon \sigma A_s T_s^4 (W) \tag{2.3}$$

Where σ represents the Stefan–Boltzmann constant ($5.670 \times 10^{-8} W/m^2 \cdot K^4$ or $0.1714 \times 10^{-8} Btu/h \cdot ft^2 \cdot R^4$). ε is emissivity, $A_s(m^2)$ is the surface area and T_s^4 (K or R) is the thermodynamic temperature of the surface.

Since radiation heat transfer is influenced by factors such as surface orientation, radiation properties, and temperatures [27], the concept of the view factor (ϕ) was introduced to account for this orientation dependency. The view factor, also referred to as the shape factor, configuration factor, or angle factor, is a geometric parameter employed in these calculations. Equations 2.4 and 2.5 show the parameters utilized.

$$\phi_{upper} = \frac{\sqrt{h_2^2 + \left(l_3 + \frac{l_1 - l_2}{2}\right)^2} - \sqrt{h_2^2 + \left(\frac{l_1 - l_2}{2}\right)^2}}{l_3} \tag{2.4}$$

$$\phi_{web} = \frac{\sqrt{h_2^2 + \left(\frac{l_1-l_2}{2}\right)^2} + (l_3 + l_1 - l_2) - \sqrt{h_2^2 + \left(l_{3+}\frac{l_1-l_2}{2}\right)^2}}{2 \times \sqrt{h_2^2 + \left(\frac{l_1-l_2}{2}\right)^2}} \tag{2.5}$$

Being h as the height and l as the width as indicated in Figure 2.1. The view factor is used in the heat flux equation shown in Equation 2.6.

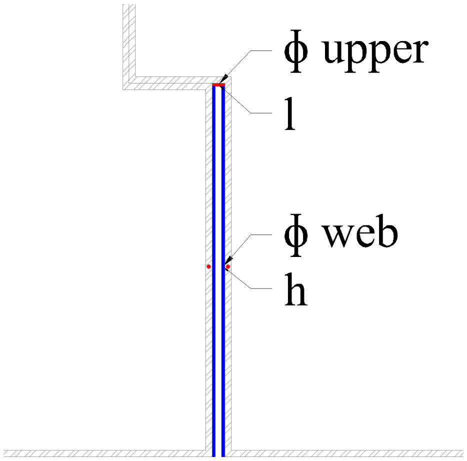

Figure 2.1: View factor represented on the model

$$k\nabla T\overrightarrow{n} = \alpha_c\left(T_g - T\right) + \phi\varepsilon_m\varepsilon_f\sigma\left(T_g^4 - T^4\right) \tag{2.6}$$

Where k is the thermal conductivity, T is the temperature, ε_m and ε_f are the emissivity of the material and the surface, respectively, and ϕ is the view factor.

2.1.4 Heating curve

As for the thermal curve of the furnace, the Equation 2.7 was taken from the ISO 834-11:2014 - Fire resistance tests [11]. The heating curve is disposed of in Figure 2.2. Where T is the temperature [ºC], and t is the time in minutes.

$$T = 345 \cdot \log_{10}(8t + 1) + 20 \tag{2.7}$$

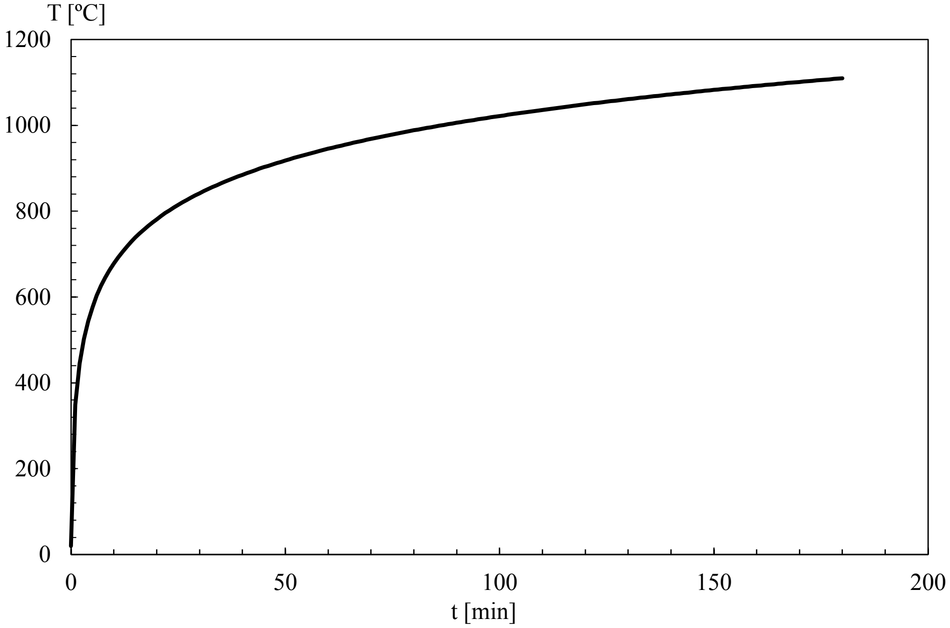

Figure 2.2: Heating Curve according to ISO 834

2.2 Material properties

2.2.1 Mechanical properties

According to the pr EN1993-1-2:2023 [30], the following Equations 2.8, 2.9 and 2.10 give the thermal expansion. Figure 2.3 illustrates the relative thermal expansion ($\Delta l/l$) during temperature of steel (θ_a) elevation, where l is the steel length at 20 ° C and Δl is the induced expansion.

For 20 °C $\leq \theta_a <$ 750 °C

$$\frac{\Delta l}{l} = 1.2 \times 10^{-5}\theta_a - 0.4 \times 10^{-8}\theta_a^2 - 2.416 \times 10^{-4} \tag{2.8}$$

For 750 °C $\leq \theta_a \leq$ 860 °C

$$\frac{\Delta l}{l} = 1.1 \times 10^{-2} \tag{2.9}$$

For 860 °C $< \theta_a \leq$ 1200 °C

$$\frac{\Delta l}{l} = 2 \times 10^{-5}\theta_a - 6.2 \times 10^{-3} \tag{2.10}$$

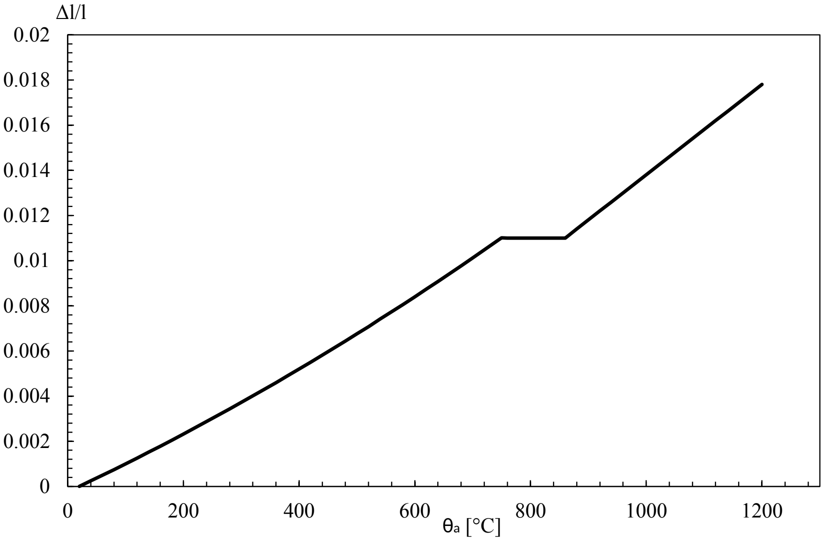

Figure 2.3: Thermal expansion of Steel

For a heating rate ranging from 2 to 50 K/min, as in the case of ISO 834 [11], pr EN1993-1-2 [30] stipulates that the properties of carbon steel, in case o this study represented by the steel deck, should be obtained under the conditions of Table 2.1 that describes the 3 main stages of carbon steel at elevated temperatures.

Table 2.1: Stress-Strain Relationship (pr EN1993-1-2 [30])

Strain range	Stress	Tangent modulus
$\varepsilon \leq \varepsilon_{p,\theta}$	$\varepsilon E_{a,\theta}$	$E_{a,\theta}$

Continued on next page

Table 2.1: Stress-Strain Relationship (pr EN1993-1-2 [30]) (Continued)

$\varepsilon_{p,\theta} < \varepsilon < \varepsilon_{y,\theta}$	$f_{p,\theta} - c + \left(\frac{b}{a}\right)\left[a^2 - (\varepsilon_{y,\theta} - \varepsilon)^2\right]^{0.5}$	$\frac{b\left(\varepsilon_{y,\theta} - \varepsilon\right)}{a\left[a^2 - \left(\varepsilon_{y,\theta} - \varepsilon\right)^2\right]^{0.5}}$
$\varepsilon_{p,\theta} \leq \varepsilon \leq \varepsilon_{y,\theta}$	$f_{y,\theta}$	0
$\varepsilon_{t,\theta} < \varepsilon < \varepsilon_{u,\theta}$	$f_{y,\theta}\left[1 - \left(\frac{\varepsilon - \varepsilon_{t,\theta}}{\varepsilon_{u,\theta} - \varepsilon_{t,\theta}}\right)\right]$	–
$\varepsilon = \varepsilon_{u,\theta}$	0.00	–
Parameters	$\varepsilon_{p,\theta} = \frac{f_{p,\theta}}{E_{a,\theta}}$__y,=0.02__t,=0.15__u,=0.20	
Function	$a^2 = (\varepsilon_{y,\theta} - \varepsilon_{p,\theta})\left(\varepsilon_{y,\theta} - \varepsilon_{p,\theta} + \frac{c}{E_{a,\theta}}\right)$ $b^2 = c\left(\varepsilon_{y,\theta} - \varepsilon_{p,\theta}\right)E_{a,\theta} + c^2$ $c = \frac{\left(f_{y,\theta} - f_{p,\theta}\right)^2}{\left(\varepsilon_{y,\theta} - \varepsilon_{p,\theta}\right)E_{a,\theta} - 2(f_{y,\theta} - f_{p,\theta})}$	

Where

$f_{y,\theta}$	is the effective yield strength
$f_{p,\theta}$	is the proportional limit
$E_{a,\theta}$	is the slope of the linear elastic range
$\varepsilon_{p,\theta}$	is the strain at the proportional limit
$\varepsilon_{y,\theta}$	is the yield strain
$\varepsilon_{t,\theta}$	is the limiting strain for yield strength
$\varepsilon_{u,\theta}$	is the ultimate strain

As the temperature increases, the resistance of carbon steel decreases, as per pr EN1993-1-2 [30]. This decline is visually represented is quantified in Table 2.3 below.

Table 2.3: Reduction Factor (pr EN1993-1-2 [30])

Reduction factors at temperature h relative to the value of f_y or E_y at 20°C

Continued on next page

Table 2.3: Reduction Factor (pr EN1993-1-2 [30]) (Continued)

°C	Reduction factor (relative to fy) for effective yield strength $k_y, \theta = \frac{f_{y,\theta}}{f_y}$	Reduction factor (relative to f_y) for proportional limit $k_p, \theta = \frac{f_{p,\theta}}{f_y}$	Reduction factor (relative to E_a) for the slope of the linear elastic range $k_E, \theta = \frac{E_{a,\theta}}{E_a}$
20	1.00	1.000	1.00
100	1.00	1.00	1.00
200	1.00	0.807	0.90
300	1.00	0.613	0.90
400	1.00	0.420	0.70
500	0.78	0.36	0.60
600	0.47	0.18	0.31
700	0.23	0.075	0.13
800	0.11	0.05	0.09
900	0.06	0.0375	0.0675
1000	0.04	0.025	0.045
1100	0.02	0.0125	0.0225
1200	0.00	0.00	0.00
NOTE: For intermediate values of the steel temperature, linear interpolation may be used.			

Applying the reduction coefficients shown in Table 2.3, the following graph stress (σ_θ) versus strain (ε_θ) in Figure 2.4 is obtained.

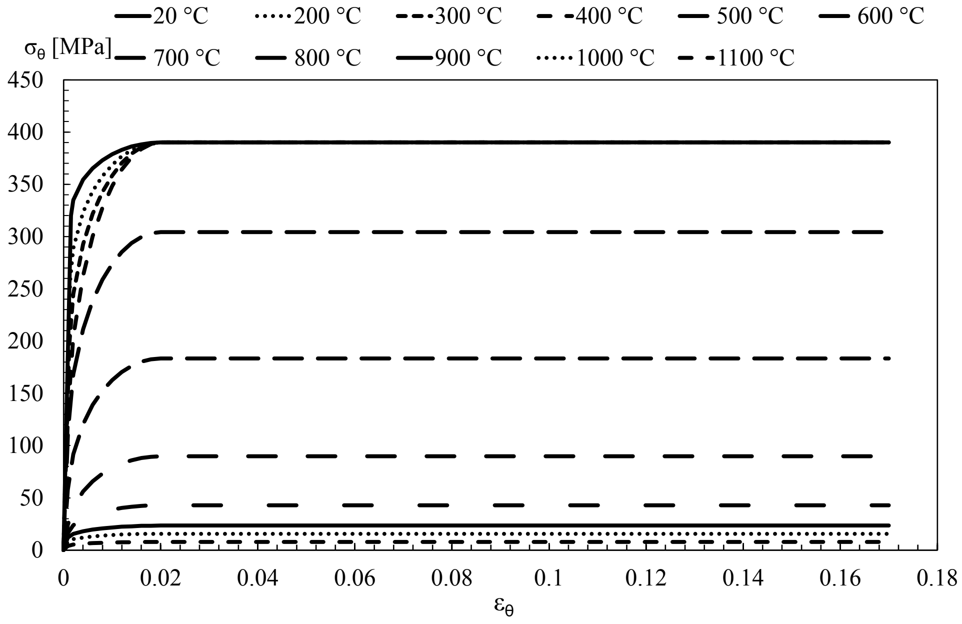

Figure 2.4: Stress x Strain curve for steel deck

About reinforcements, they adhere to analogous principles as those employed on the steel deck. It has distinct reduction coefficients governing their behavior, as presented in Table 2.4 extracted from pr EN1992-1-2 [31].

Table 2.4: Reduction Factor (pr EN1992-1-2 [31])

Reduction factors at elevated temperatures			
°C	$k_y, \theta = \frac{f_{y,\theta}}{f_y}$	$k_p, \theta = \frac{f_{p,\theta}}{f_y}$	$k_E, \theta = \frac{E_{a,\theta}}{E_a}$
20	1.000	1.000	1.000
100	1.00	0.96	1.00
200	1.00	0.92	0.87
300	1.00	0.81	0.72
400	0.94	0.63	0.56

Continued on next page

Table 2.4: Reduction Factor (pr EN1992-1-2 [31]) (Continued)

500	0.67	0.44	0.40
600	0.40	0.26	0.24
700	0.12	0.08	0.08
800	0.11	0.06	0.06
900	0.08	0.05	0.05
1000	0.05	0.03	0.03
1100	0.03	0.02	0.02
1200	0.000	0.000	0.000
NOTE: For intermediate values of the steel temperature, linear interpolation may be used.			

The reduction in the Stress versus Strain in the reinforcement at elevated temperatures is illustrated in Figure 2.5.

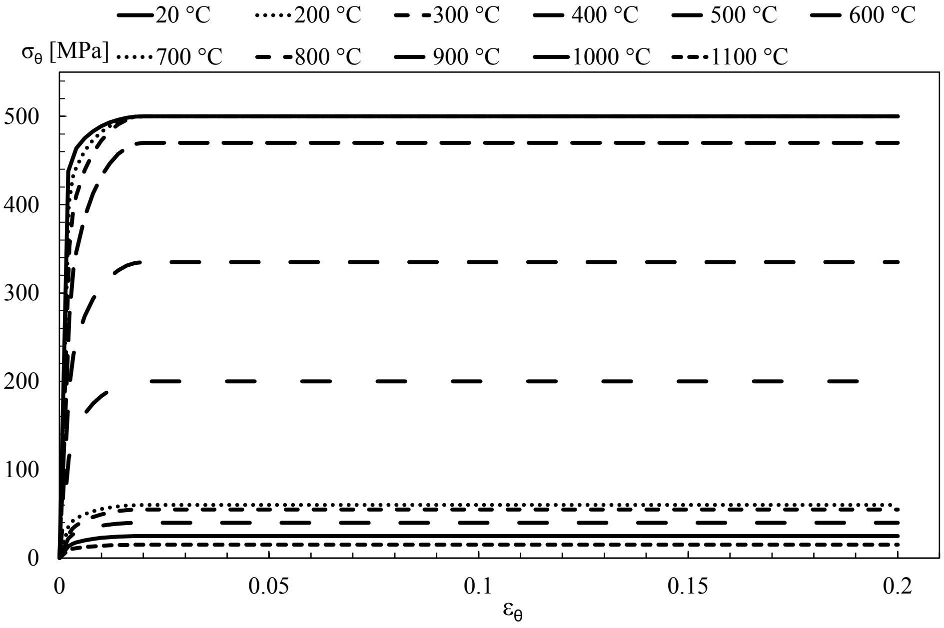

Figure 2.5: Stress x Strain curve for reiforcement steel

The following equations may be used to determine the thermal expansion $\Delta l/l$ of normal weight concrete with siliceous aggregates.

For 20 °C $\leq \theta_c \leq$ 805 °C

$$\frac{\Delta l}{l} = -1.2 \times 10^{-4} + 6 \times 10^{-6}\theta_c + 1.4 \times 10^{-11}\theta_c^3 \tag{2.11}$$

For 805 °C $< \theta_c \leq$ 1200 °C

$$\frac{\Delta l}{l} = 12 \times 10^{-3} \tag{2.12}$$

Where l represents the length at 20 °C in meters, Δl defines the temperature-induced expansion of the concrete, and θ_c denotes the concrete temperature in degrees Celsius.

The Thermal Expansion at elevated temperatures is illustrated in Figure 2.6.

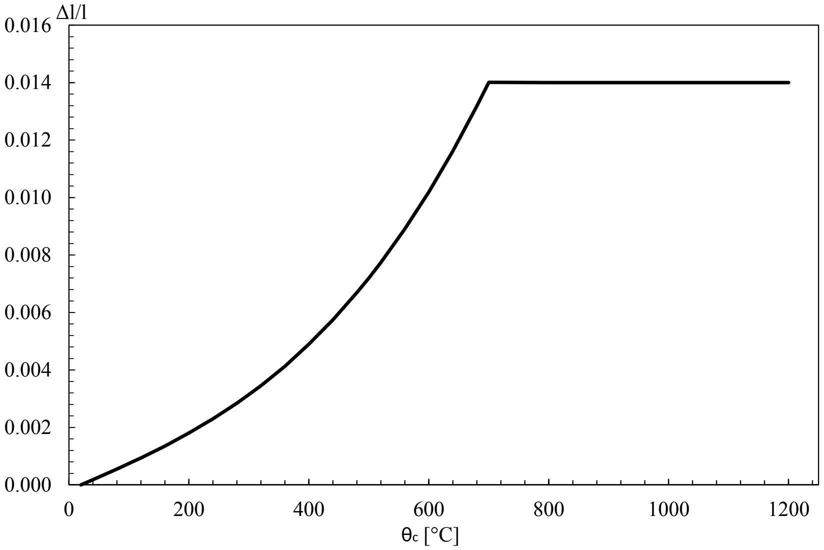

Figure 2.6: Thermal expansion for concrete

The stress-strain behavior of concrete at elevated temperatures, pr EN1992-1-2 [31] outlines a table defining the reduction factors. This study specifically employs concrete characterized by silicon aggregates.

For $\varepsilon_c \leq \varepsilon_{c1,\theta}$

$$\sigma_c\left(\theta\right) = \frac{3\varepsilon_c \times f_{c,\theta}}{\varepsilon_{c1,\theta}\left(2 + \left(\frac{\varepsilon_c}{\varepsilon_{c1,\theta}}\right)^3\right)} \tag{2.13}$$

Table 2.5: Reduction factor (pr EN1992-1-2 [31])

Reduction factors at elevated temperatures			
°C	$k_c, \theta = \frac{f_{c,\theta}}{f_{ck}}$	$\varepsilon_{c1,\theta}$	$\varepsilon_{cu1,\theta}$
20	1.00	0.0025	0.002
100	1.00	0.004	0.0225
200	0.95	0.0055	0.025
300	0.85	0.007	0.0275
400	0.75	0.01	0.03
500	0.6	0.015	0.0325
600	0.45	0.025	0.035
700	0.3	0.025	0.0375
800	0.15	0.025	0.04
900	0.08	0.025	0.0425
1000	0.04	0.025	0.0425
1100	0.01	0.025	0.00475
1200	0.000	0.000	0.000
NOTE: For numerical purposes, a descending branch may be used. Linear or non-linear models may be used for $\varepsilon_{c1,\theta}$ $\varepsilon_c \leq \varepsilon_{cu1,\theta}$			

Figure 2.7 visually represents the stress versus strain curve, derived from Equation 2.13

and incorporating reduction factors from Table 2.5.

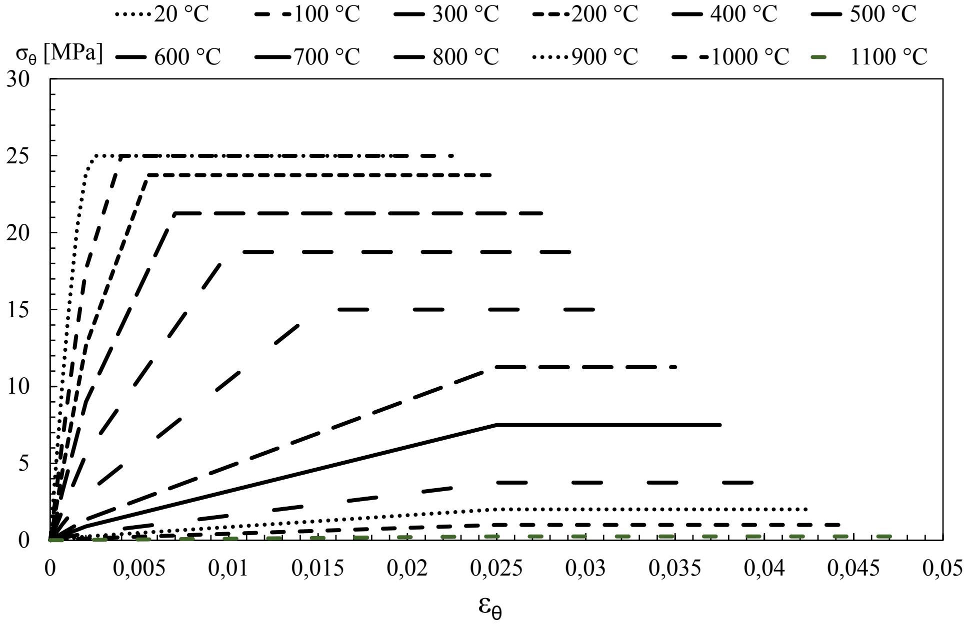

Figure 2.7: Stress x Strain curve for concrete C25/30

The descending curves of both concrete and steel are not represented in the stress-strain curves due to the construction model used and the parameters accepted by the software.

2.2.2 Thermal properties

Steel

The steel properties used in this dissertation were sourced from pr EN1993-1-2 [30], a standard that outlines the thermal properties of steel for use in construction and structural reinforcement according to the steel temperature (θ_a). The equations employed for calculating these properties are presented below.

Following the pr EN1993-1-2 [30] the density (ρ) of steel is 7850 kg/m^3 2.14 and shall be considered independent of the temperature, as shown in Figure 2.8.

$$\rho = 7850 \left[\frac{kg}{m^3}\right] \tag{2.14}$$

The specific heat (c_a) was determined by the Equations 2.15 to 2.18 and illustrated in Figure 2.8:

For 20 °C $\leq \theta_a <$ 600 °C

$$c_a = 425 + 7.73 \times 10^{-1}\theta_a - 1.69 \times 10^{-3}\theta_a^2 + 2.22 \times 10^{-6}\theta_a^3 \left[\frac{J}{kgK}\right] \tag{2.15}$$

For 600 °C $\leq \theta_a <$ 735 °C

$$c_a = 666 + \frac{13002}{738 - \theta_a} \left[\frac{J}{kgK}\right] \tag{2.16}$$

For 735 °C $\leq \theta_a <$ 900 °C

$$c_a = 545 + \frac{17820}{\theta_a - 731} \left[\frac{J}{kgK}\right] \tag{2.17}$$

For 900 °C $\leq \theta_a \leq$ 1200 °C

$$c_a = 650 \left[\frac{J}{kgK}\right] \tag{2.18}$$

For thermal conductivity (λ_a), the Equations 2.19 and 2.20 used and the constant obtained are presented below and illustrated in Figure 2.8:

For 20 °C $\leq \theta_a <$ 800 °C

$$\lambda_a = 54 - 3.33 \times 10^{-2}\theta_a \left[\frac{W}{mK}\right] \tag{2.19}$$

For 800 °C $\leq \theta_a \leq$ 1200 °C

$$\lambda_a = 27.3 \left[\frac{W}{mK}\right] \tag{2.20}$$

Figure 2.8 illustrates the thermal properties of steel according to temperature.

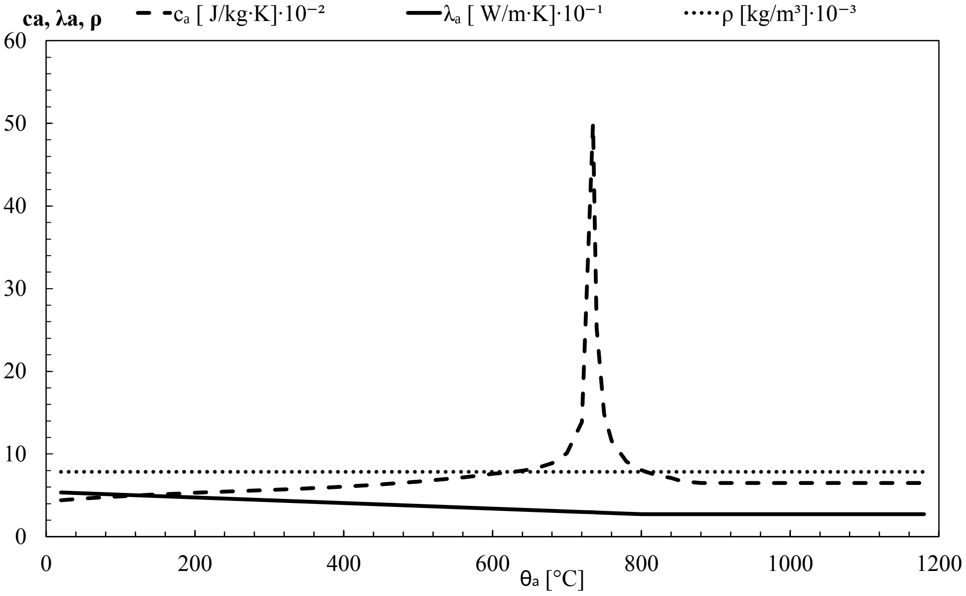

Figure 2.8: Thermal properties of steel

Concrete

The properties of the concrete used in this study are based on normal weight concrete (NWC), which is also commonly referred to as conventional concrete. These properties can be found in pr EN1992-1-2 [31] and varies according to the concrete's temperature (θ_c) .

The Equations 2.21 to 2.24 used in this dissertation were obtained from pr EN1992-1-2 [31] for the specific heat (c_c).

For 20 °C $\leq \theta_c \leq$ 100 °C

$$c_c = 900 \left[\frac{J}{kgK}\right] \tag{2.21}$$

For 100 °C $< \theta_c \leq$ 200 °C

$$c_c = 900 + (\theta_c - 100) \left[\frac{J}{kgK}\right] \tag{2.22}$$

For 200 °C $< \theta_c \leq$ 400 °C

$$c_c = 900 + \frac{(\theta_c - 100)}{2} \left[\frac{J}{kgK}\right] \tag{2.23}$$

For 400 °C $< \theta_c \leq$ 1200 °C

$$c_c = 900 + \frac{(\theta_c - 100)}{2} \left[\frac{J}{kgK}\right] \tag{2.24}$$

$$c_{c.peak} = 2020 \left[\frac{J}{kgK}\right] \tag{2.25}$$

According to pr EN1992-1-2 [31], the specific heat of the concrete must be considered as a constant between the temperatures of 100 °C and 115 °C due to evaporation of the water and calculated with a linear decrease between 115 °C and 200 °C. In this thesis, the moisture content of the concrete will be assumed to be 3%, based on the information provided in the manufacturer's [26].

Regarding thermal conductivity (λ_c), the Equations 2.26 to 2.28 utilized in this thesis were extracted from pr EN1992-1-2, as demonstrated below.

For $\theta_c \leq$ 140 °C

$$\lambda_c = 2 - 0.2451 \times \left(\frac{\theta_c}{100}\right) + 0.0107 \times \left(\frac{\theta_c}{100}\right)^2 \left[\frac{W}{mK}\right] \tag{2.26}$$

For 140 °C $< \theta_c <$ 160 °C

$$\lambda_c = -0.02604\theta_c + 5.324 \left[\frac{W}{mK}\right] \tag{2.27}$$

For 160 °C $\leq \theta_c \leq$ 1200 °C

$$\lambda_c = 1.36 - 0.136 \times \left(\frac{\theta_c}{100}\right) + 0.0057 \times \left(\frac{\theta_c}{100}\right)^2 \left[\frac{W}{mK}\right] \tag{2.28}$$

Regarding the density (ρ) of normal-weight concrete, it is noted in pr EN1992-1-2 [31] that in the event of a fire, the concrete experiences a reduction in moisture content, which consequently affects its density. The standard defines that the density of normal-weight concrete ranges between 2000 (kg/m^3) and 2600 (kg/m^3), for this thesis, the density used was 2300 (kg/m^3). Figure 2.9 illustrates density, specific heat with moisture in 3%, and thermal conductivity.

For 20 °C $\leq \theta_c \leq$ 115 °C

$$\rho(\theta_c) = \rho(20°C) \left[\frac{kg}{m^3}\right] \tag{2.29}$$

For 115 °C $< \theta_c \leq$ 200 °C

$$\rho(\theta_c) = \rho(20°C) \times 1 - 0.02 \times \frac{\theta_c - 15}{85} \left[\frac{kg}{m^3}\right] \tag{2.30}$$

For 200 °C $< \theta_c \leq$ 400 °C

$$\rho(\theta_c) = \rho(20°C) \times 0.98 - 0.03 \times \frac{\theta_c - 200}{200} \left[\frac{kg}{m^3}\right] \tag{2.31}$$

For 400 °C $\theta_c \leq$ 1200 °C

$$\rho(\theta_c) = \rho(20°C) \times 0.95 - 0.07 \times \frac{\theta_c - 400}{800} \left[\frac{kg}{m^3}\right] \tag{2.32}$$

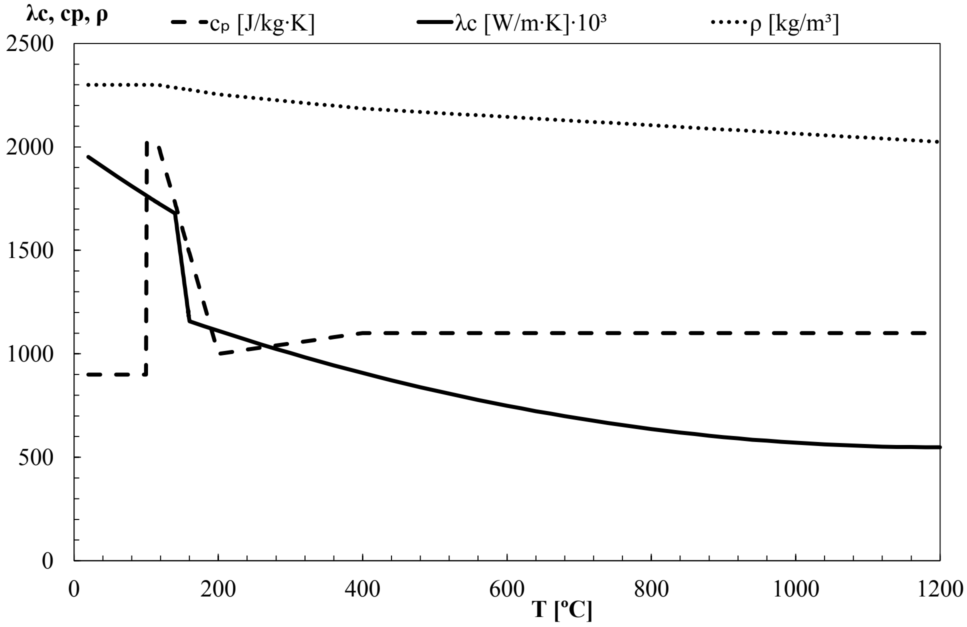

Figure 2.9: Concrete thermal properties

Air

The thermal properties of air are not disposed on any normative, so it was necessary to browse on bibliography. The data given by Engel [27] are based on experimental results and are presented in Table 2.6 and Figure 2.10 illustrates the thermal properties of air at elevated temperatures. These properties will be implemented in the numerical model as part of the simulation. During the initial minutes of the fire, the steel deck and the concrete suffer a separation, creating air layers that act as a thermal barrier. The air layer was implemented inside the shell element with a thickness of one millimeter.

Table 2.6: Air properties according to the temperature

Temperature T [°C]	Density $\rho \left[\frac{kg}{m^3}\right]$	Specific Heat $c_a \left[\frac{J}{kgK}\right]$	Thermal Conductivity $\lambda_a \left[\frac{W}{mK}\right]$
0	1.292	1.006	0.2364
10	1.246	1.006	0.2439
20	1.204	1.007	0.2514
30	1.164	1.007	0.2588
40	1.127	1.007	0.2662
50	1.092	1.007	0.2735
100	0.9458	1.009	0.3095
200	0.7459	1.023	0.3779
400	0.5243	1.069	0.5015
600	0.4042	1.115	0.6093
800	0.3289	1.153	0.7037
1000	0.2772	1.184	0.7868
1200	0.2299	1.214	0.8674

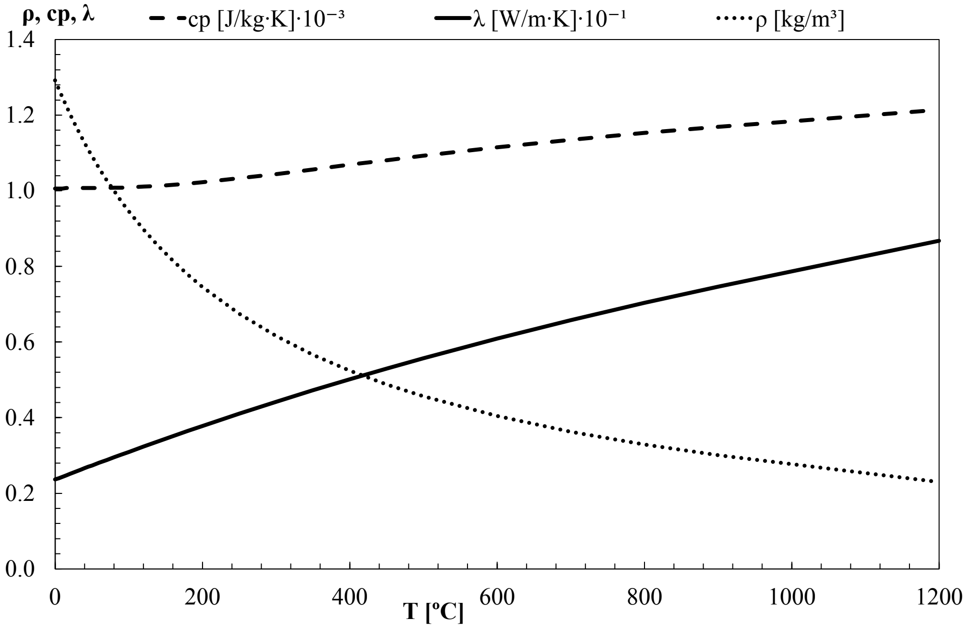

Figure 2.10: Air thermal properties

Mineral wool

To prevent fire from spreading to the structure, the numerical simulation incorporates mineral wool insulation with a 50 kg/m^3 density. The thermal properties of the mineral wool have been derived from pr EN1995-1-2 [32]. The variations in the properties of mineral wool are presented in Table 2.7 and visually depicted in Figure 2.11.

Table 2.7: Mineral Wool properties according to the temperature

°C	Thermal Conductivity $\lambda_a \left[\frac{W}{mK}\right]$	$c_a \left[\frac{J}{kgK}\right]$	ρ/ρ_{20}	Density $\rho \left[\frac{kg}{m^3}\right]$
20	0.036	880	1	50
100	0.047	1040	1	50
200	0.06075	1160	0.98	49
400	0.252	1280	0.977	48.85

Continued on next page

Table 2.7: Mineral Wool properties according to the temperature (Continued)

600	0.4204	1350	0.973	48.65
800	0.6446	1430	0.97	48.5
925	0.8408	1470	0.96	48
1200	1.2613	1580	0.887	44.35

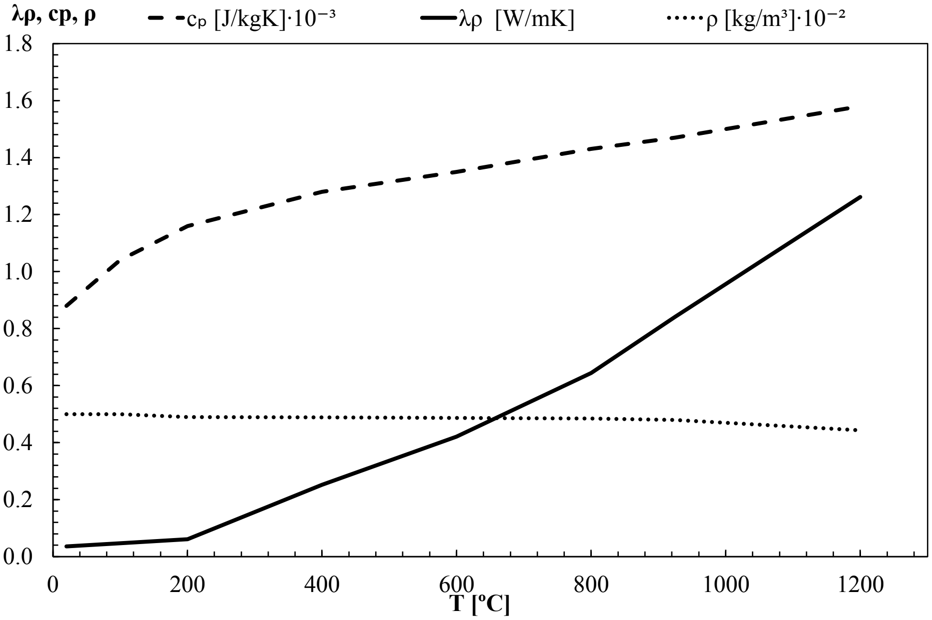

Figure 2.11: Mineral Wool Properties

Chapter 3

Methodology

The thermal and mechanical simulations were conducted using the software ANSYS Mechanical APDL and, according to availability, three different finite elements were chosen for each type of simulation. In the thermal model, the finite elements were Shell 131 for the steel deck, Link 33 for the reinforcement and steel mesh, using different cross-sectional areas, and Solid 70 to represent the Mineral Wool and Concrete. The finite element software used in this dissertation is ANSYS Mechanical APDL.

3.1 Thermal analysis methodology

3.1.1 Finite elements

In this section, it is described the elements that were used to represent the materials in the thermal simulations. The finite elements were selected based on their availability in the software and their accuracy in representing the physical properties of the materials.

Shell 131 is a 3D element with thermal conduction on the plane of the element and through its thickness. The element has 4 nodes, and each node has up to 32 temperature degrees of freedom. This three-dimensional element is used in thermal simulations and generates temperatures that can be passed to structural shell elements. The element employs linear interpolation functions in the plane with a complete Gauss integration method (2 × 2), along with linear interpolation using three Gauss points in its thickness. Figure 3.2 represents the element in the ANSYS model.

This element can create multiple layers with different thicknesses and properties. These layers can be used to simulate the formation of an air layer resulting from the displacement between the steel deck and the concrete or mineral wool during fire exposure as represented by 3.2 and 3.1, being the layer 1, air and layer 2, steel.

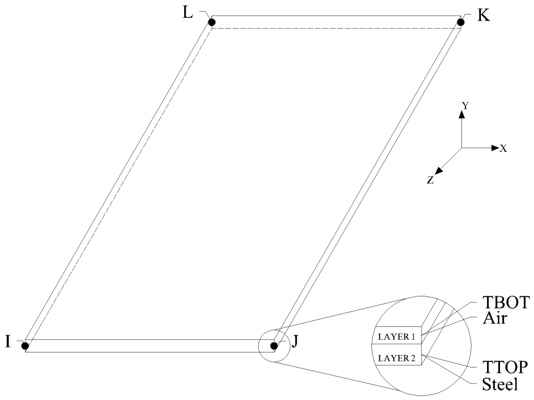

Figure 3.1: Shell 131 geometry

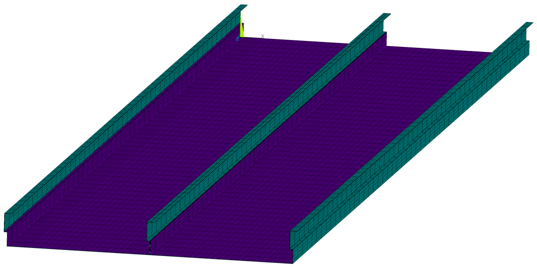

Figure 3.2: Steel Deck in ANSYS

Solid 70 is an eight-node 3D element with a single degree of freedom at each node. This element has been selected for this analysis due to the applicability of transient thermal analysis. The element represents the concrete in the thermal analysis, and isotropic properties have been defined for the thermal model. This element uses a linear interpolation function and a full Gauss integration scheme (2 × 2 × 2). Figure 3.3 represents the geometry of Solid 70 and Figures 3.5 and 3.4 represent concrete and mineral wool in ANSYS, respectively.

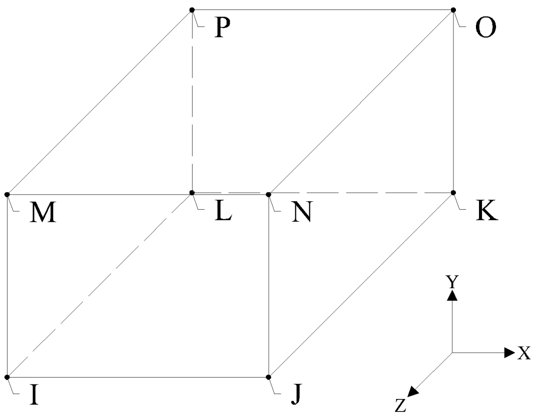

Figure 3.3: Solid 70 geometry

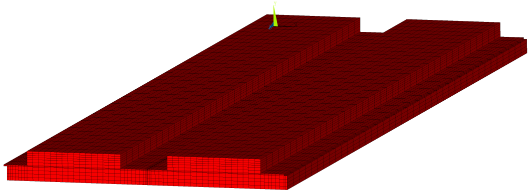

Figure 3.4: Mineral wool in ANSYS

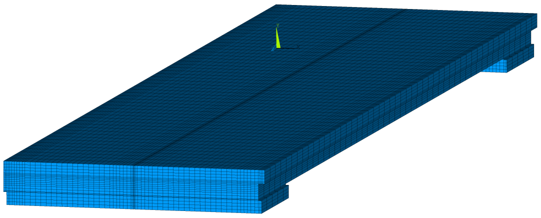

Figure 3.5: Concrete in ANSYS

Link 33 is a three-dimensional element that can transfer heat between its nodes, having only one degree of freedom for temperature at each node. The heat is transferred between the nodal points. In the thermal model, Link 33 represents the reinforcement bar and the steel mesh, each with different cross-sectional areas. Figure 3.6 shows the node description for the element.

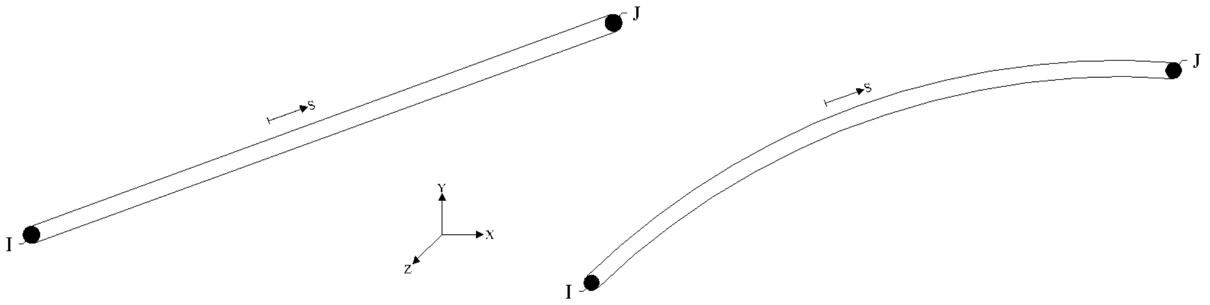

Figure 3.6: Link 33 node description

The representation of the rebars and the mesh used against the cracks are shown in Figures 3.7 and 3.8.

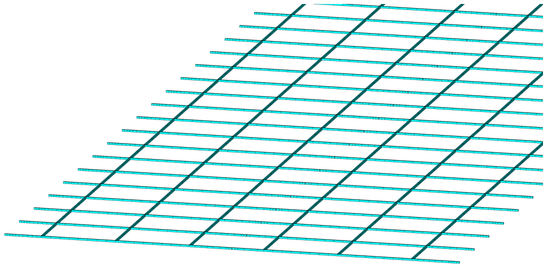

Figure 3.7: Mesh - Link 33 in ANSYS

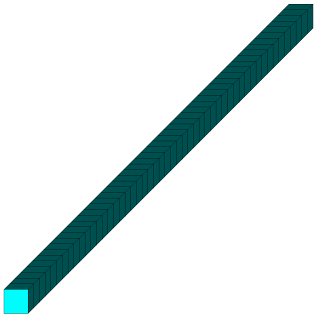

Figure 3.8: Rebar - Link 33 in ANSYS

The nodes from these elements are in perfect contact with the concrete, sharing the same nodes from Solid 70.

3.1.2 Thermal model calculation

The thermal model employs a 3D nonlinear transient thermal analysis. The software calculates heat transfer using Equation 3.1 and previously shown Equation 2.6. These equations are represented in differential form, enabling the simulation of heat conduction in materials. Boundary conditions are defined by the equality between the heat flux arriving at the surface due to convection and radiation.

$$k\nabla^2 T + q = \rho C \frac{\partial T}{\partial t} \tag{3.1}$$

Where k is the thermal conductivity, ρ is the density, C is the specific heat of the material, q is the heat transfer rate, T is the temperature, t is the time. The time t in Equation 3.1 requires the use of an incremental solution and the temperature requires an iterative procedure for each time increment.

3.1.3 Boundary conditions

Boundary conditions have the function of defining the behavior of the mathematical model within a specific domain during the simulation period. As the thermal simulation only involves heat exchanges from a bottom-up heat source simulating fire and does not entail any applied load on the structure, constraints were not required to prevent displacements and rotations. However, this situation had to be altered for the thermal-mechanical simulation.

Convection

For the convection parameters, the recommended values were extracted from the EN 1991-1-2 standard (2002) [33], as heat transfers affected by radiation are assumed. Therefore, the convection coefficient applied to the unexposed surface is α_c =9 $[W/m^2K]$ to include the radiation effect. On the other hand, the convection coefficient for heat transfer on the exposed face affected by the ISO 834 heat curve is α_c =25 $[W/m^2K]$. These values align with those used in the report that served as the basis for the thesis. The configuration of the convection coefficient distribution is represented in Figure 3.9.

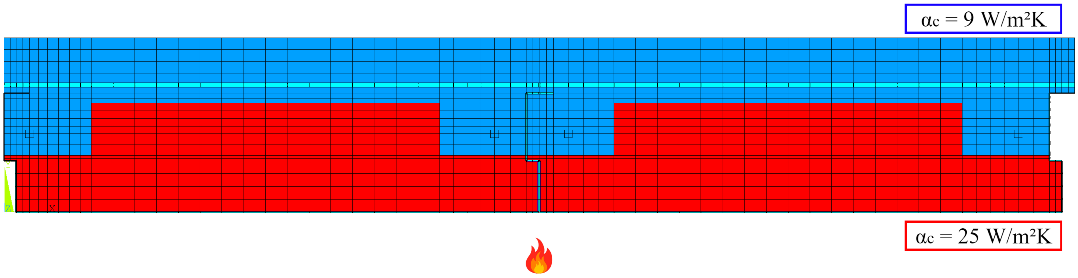

Figure 3.9: Convection distribution

To represent the boundary conditions existing in the 2mm gap between the two steel decks, a convection coefficient of α_c =25 $[W/m^2K]$ was also implemented, assuming these areas are directly exposed to fire. This is represented in Figure 3.10

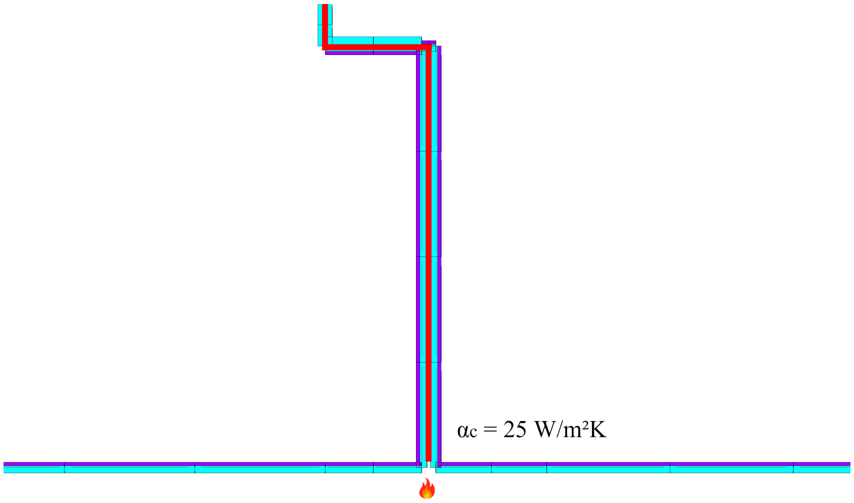

Figure 3.10: Convection Gap

Radiation

The emissivity (ε) of a material varies depending on its composition and surface characteristics. This property is crucial in calculating non-contact temperature measurements and heat transfer. The equation that prescribes this heat exchange between two surfaces without considering the distance between the surfaces is illustrated in Equation 3.2.

$$\varepsilon = \frac{Energy\ emitted\ by\ a\ surface}{Energy\ emitted\ by\ a\ black\ body\ at\ same\ temperature} \tag{3.2}$$

In the Mechanical APDL software, surfaces are assumed to be Gray Diffuse, implying that absorptivity equals emissivity, and emissivity plus reflectivity equals one. Energy transfer between two surfaces is calculated using the Stefan-Boltzmann Law, which states that heat transfer depends on the emitting surface's area and emissivity, the two surfaces' absolute temperature, and the orientation angle between them. This heat exchange is represented by Equation 2.3.

As prescribed by EN 1991-1-2 [33] the concrete's emissivity is assumed as $\varepsilon_m = 0.7$, but, as the concrete is not directly exposed to fire is not going to be used. The steel emissivity is assumed as $\varepsilon_m = 0.5$, once the steel deck as a zinc layer on it's surface. The emissivity of the fire is assumed as $\varepsilon_f = 1$.

For the underside of the steel deck, a flame emissivity value of ε_f=1.0 was utilized. However, for the space created by the connection of the two decks, where heat transfer is limited due to geometry, a value of $\phi \cdot \varepsilon_f$=0.5 was adopted. These boundary conditions are represented in the Figure 3.11

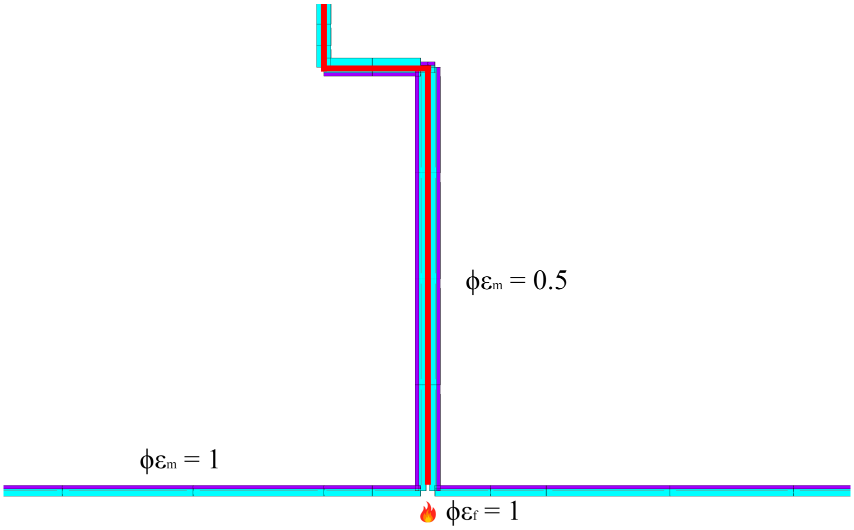

Figure 3.11: Representation of the boundary conditions for emissivity

3.1.4 Solution controls

The thermal analysis conducted for this thesis employed transient analysis, which computes the system's response over a defined period of time. The analysis time was set to 7200 seconds, equivalent to 2 hours, mirroring the laboratory experiment. For the Time Control, a 'Time increment' was defined with a Time step size of 60, with a minimum time step of 1 and a maximum of 60 seconds. This setup means that if the solution converges in the first attempt, the time increment will be 60 seconds. If the time step size reaches 1 and convergence is still not attained, the solution will terminate. For the accuracy of the results, all the results were saved, for every time step. The convergence parameters for the iterative process adopted a heat flow with a tolerance of 1×10^{-3} and a minimum reference value of 1×10^{-6} (W).

3.2 Mechanical simulation methodology

In the mechanical simulation, the following materials were utilized to represent the steel deck, reinforcement bars, and concrete. As the mineral wool has no mechanical strength, this element will not be used in the mechanical simulation. The air gap between the slab and the concrete or mineral wool, depending on the location, was also deleted, as air possesses no mechanical properties.

3.2.1 Finite elements

The change of element type for the mechanical simulation was performed using the element type change command from thermal to structural, where the software converts to the corresponding elements. The Shell 131 was transformed into Shell 181, excluding the air gap layer. Link 33 was transformed into Link 180, assigning section areas according to those provided in the reference [26]. Lastly, Solid 70 was transformed into Solid 185, with mechanical properties assigned to the material representing the concrete.

Shell 181 element is adequate to analyze with thin to moderated thick shell structures.

It is a four-node element with four to six degrees of freedom on each node, these being, translations in x, y, and z directions and rotations about x, y, and z-axes. In the context of this study, the element is configured with the default characteristic on ANSYS, bending and membrane. The integration option "full with incompatible" was selected. The element will represent the steel deck and is equivalent to Shell 131 in the thermal model. Figure 3.12 illustrates the Shell 181 element. This element uses linear interpolating function with full integration Gauss method in the plane of the element and five integration points over thickness.

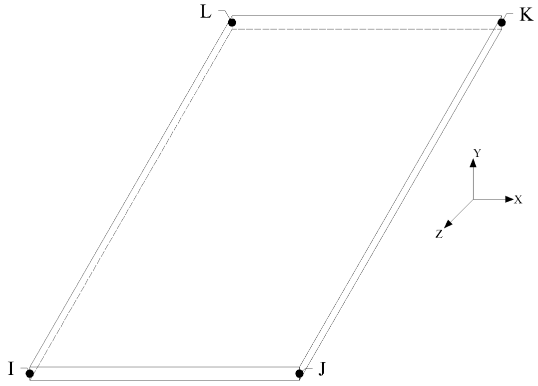

Figure 3.12: Shell 181

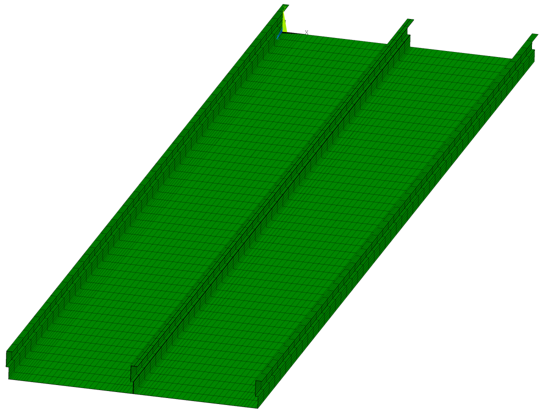

Figure 3.13: Steel Deck

Link 180 is a three-dimensional spar that can be used to model trusses, sagging cables, links, springs, and many other engineering applications. Link 180 is a uniaxial tension-compression element and has three degrees of freedom at each node, being, translations in nodal x, y, and z directions. It supports stress-stiffness terms encompassing large-deflection effects, and it supports various material models, including elastic isotropic hardening plasticity, isotropic hardening plasticity, kinematic hardening plasticity, Hill anisotropic plasticity, and Chaboche nonlinear hardening plasticity. This element represents the reinforcement bar in the mechanical model and is equivalent to Link 33 in the thermal model. Figure 3.14 illustrates Link 180 and Figure 3.15 in the ANSYS model.

This element uses linear interpolating functions with one Gauss integration point.

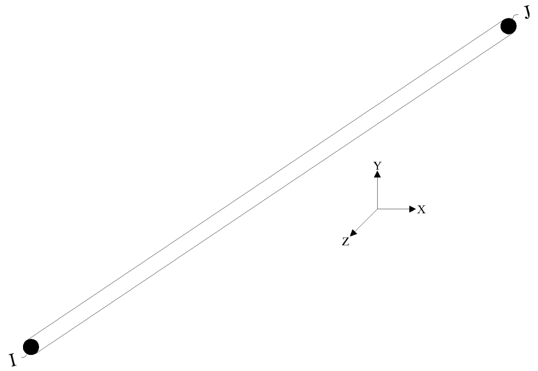

Figure 3.14: Link 180

Figure 3.15: Rebar

The link 180 element type is also used for the reinforcement mesh with $\phi = 5.5mm$ that is used to prevent small cracks in the concrete during the event of fire. This mesh is illustrated in Figure 3.16, and is superposed to the concrete finite element mesh.

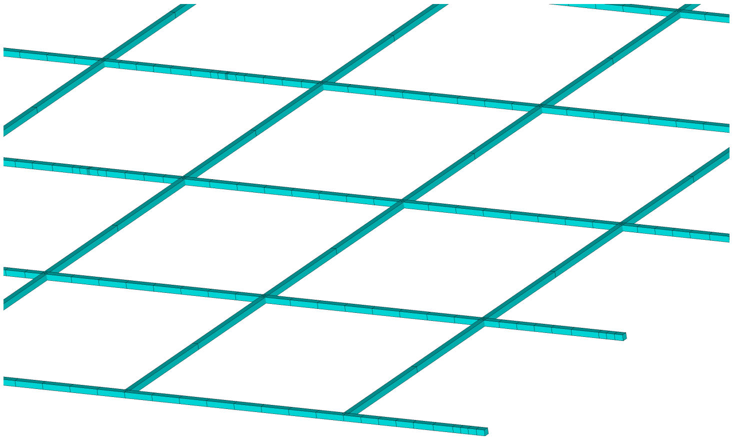

Figure 3.16: Mesh reinforcement

Solid is a 3D element used to design solid structures, such as representing the concrete in the mechanical simulation. The element has three degrees of freedom, translations in the nodal x, y, and z directions. It also can simulate deformations of nearly incompressible elastoplastic materials. Figure 3.17 illustrates Solid 185 geometry and Figure 3.18 illustrates the concrete in ANSYS.

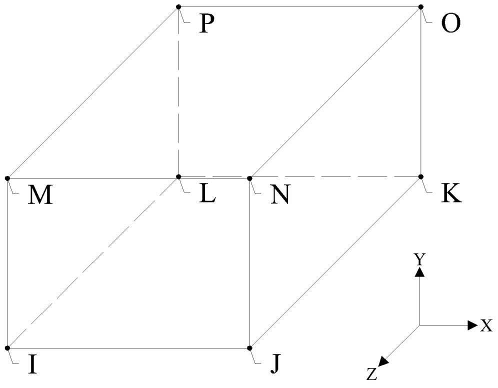

Figure 3.17: Solid 185

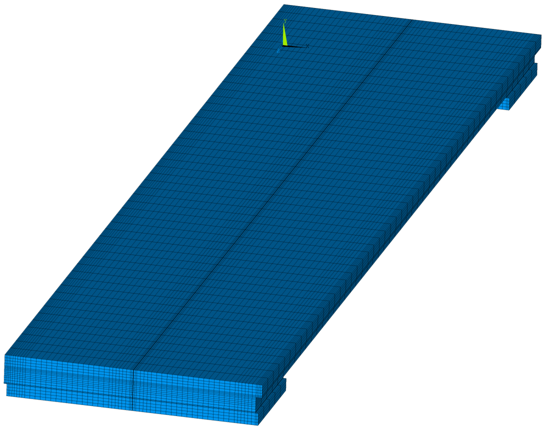

Figure 3.18: Concrete

3.2.2 Simplified calculation method

For calculating the sagging resistance moment $M_{fi,t,Rd}$, the simplified calculation method presented in Annex D in the EN 1994-1-2 [34] was used. Since the slab's geometry does not have a specific method represented in the standard, minor adaptations were made to predict the load-bearing capacity of the slab.

For the calculation of the design resisting moment, the concrete, steel bars, and steel plate components were individually assessed to determine their respective areas and subsequent resistant stresses. Afterward, the position of the neutral axis was determined using Equation 3.3 to find the area of compressed concrete. Finally, using the centroids of each element, as shown in Figure 3.20, the slab's resisting moment was calculated. The flowchart shown in Figure 3.19 illustrates the process for obtaining this moment.

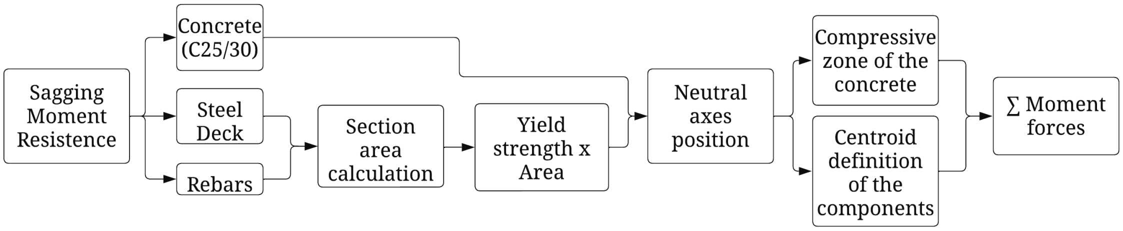

Figure 3.19: Sagging moment resistance calculation

The forces exerted by each component, multiplied by the quantity of each element present in the slab, are shown in Figure 3.21. The position of each component are illustrated in Figure 3.20.

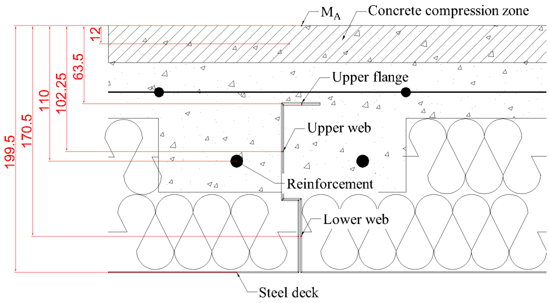

Figure 3.20: Cross-section of centroids

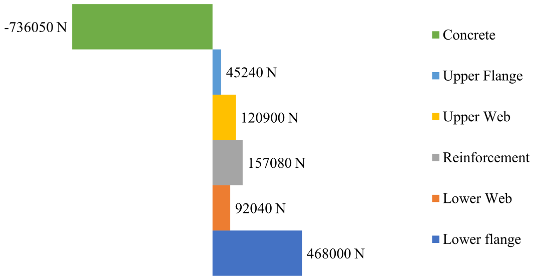

Figure 3.21: Force of the components

For calculating the position of the plastic neutral axis of the concrete, the method of equilibrium of horizontal forces on the slab section was employed, as described by Equation 3.3.

$$z_{pl} = \alpha_{slab} \cdot l \cdot f_c \cdot \sum F_i \tag{3.3}$$

Being l the total width of the slab, f_c the compressive strength of the concrete, and z_{pl} the distance of the plastic neutral axis from a reference point.

After the determination of the plastic neutral axes of the concrete, the moment resistance $M_{fi,tRd}$ of the slab was calculated according to the Equation 3.4.

$$M_{fi,tRd} = \sum_{i=1}^{n} A_i z_i k_{y,\theta,i} \left(\frac{f_{y,i}}{\gamma_{M,fi}} \right) + \alpha_{slab} \sum_{j=1}^{m} A_j z_j k_{c,\theta,j} \left(\frac{f_{c,j}}{\gamma_{M,fi,c}} \right) \tag{3.4}$$

Where z_i and z_j are the distance from the plastic neutral axis to the centroid of the elemental area A_i or A_j.

Both equations 3.3 and 3.4 were adapted from the calculation procedure performed by ArcelorMittal [35] for composite structures.

3.2.3 Support conditions

For the support conditions used in the simple supported slab, zero displacements were applied to the lines of nodes corresponding to the supporting interfaces, representing the connection of the slab to a beam. At one end, displacements in the X and Y directions were constrained, while at the other end, displacements in the X, Y, and Z directions were constrained, thus forming a statically determinate element. These support conditions are demonstrated in Figure 3.22.

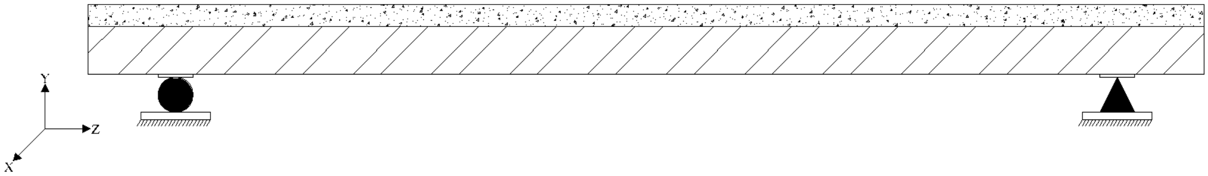

Figure 3.22: Support conditions

3.2.4 Load application

Regarding the force applied to conduct the load-bearing capacity test of the slab, the force was used in the form of table for incremental solution method. This means that a proportional load increment is applied to the slab with each time increment. Following the recommendation of EN 1994-1-1, two interface surfaces were used to represent the bearing load plates, which are located at L/4 meters from the support, where L represents the span length. In his case, the span length is 4.4 meters. Figure 3.23 and 3.24 illustrate the mode of incremental load application on the slab.

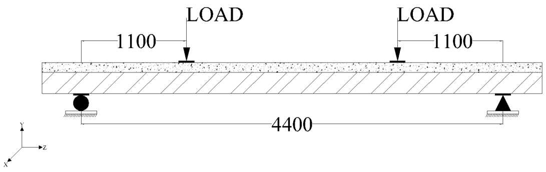

Figure 3.23: Load application

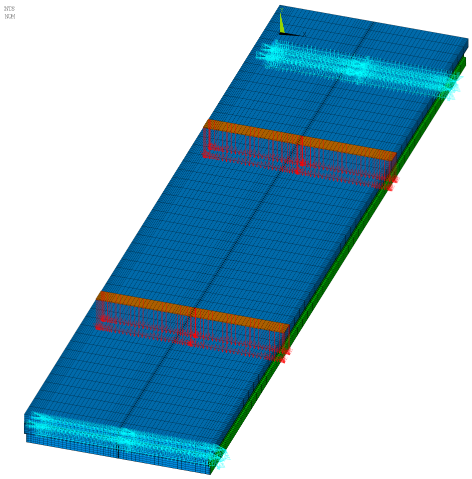

Figure 3.24: Load application ANSYS

After calculating the bending moment, it was possible to estimate the soliciting action in the structure. This estimation is made according to the structural system prescribed by pr EN1994-1-2 [34] for flexural tests. In this case, the slab is conceived as an isostatic structure supported on both sides and receives the load at one-quarter of the span, as illustrated in Figure 3.25. Considering the span of 4.4 meters, the force is applied at 1.1 meters from each support. The section between the applied forces is subjected to constant bending, and the bending moment is given by Equation 3.5.

$$M = load \times 1.1 \tag{3.5}$$

Being the load applied and 1.1 is the distance between the point load application and the slab's support.

The moment diagram of a cross-section of the slab is shown in Figure 3.25.

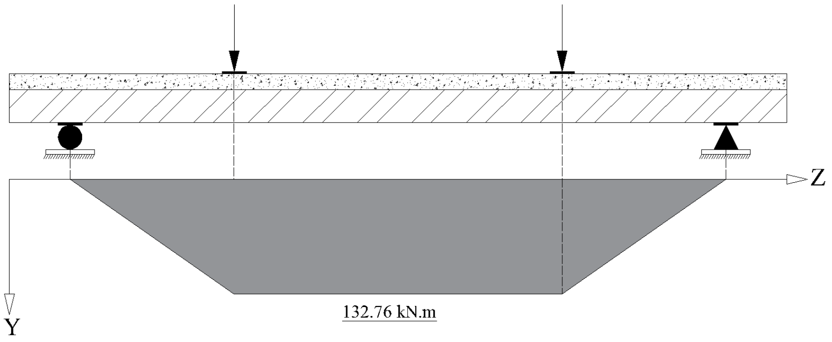

Figure 3.25: Moment diagram

3.2.5 Solution controls

In the mechanical simulation, the chosen method was structural static analysis, with the Large Displacement Static option. This signifies that the program is designed to undertake a nonlinear static analysis, including the effects of significant deformations.

For time control parameters, the end of the load step was set to 1200 seconds. The time increment was selected as the method of time control, with a time step size of 50 seconds, a minimum time step of 0.001, and a maximum time step of 75 seconds.

The program initially seeks an equilibrium position using a time of 50 seconds in the analytical process. If it fails to achieve equilibrium, the program automatically employs a bisection method, progressively reducing the applied time or load on the slab until an equilibrium position is attained. To ensure precision, all substeps were written.

3.3 Thermal structural analysis

After validating the temperatures in the numerical simulation based on the reference [26], thermo-mechanical simulations were conducted by applying load to the structure to measure its mechanical resistance under fire conditions. The parameters and how the model was processed are detailed in this section.

3.3.1 Thermal and mechanical properties

The thermo-mechanical properties used in this dissertation were extracted from pr EN 1992-1-2 [31]. They mostly include reduction coefficients for their respective strengths as temperature increases, which can even reach 0 at temperatures above 1100 degrees Celsius, in the case of steel.

3.3.2 Analytical calculation method

Using the temperatures determined in the thermal analysis, it was possible to get the nodal temperatures of all elements that contribute to the structural resistance of the slab. This temperatures are listed in Table 3.1

Table 3.1: Component temperatures

Location	30min	60min	90min	120min
Lower Deck	767.41	889.01	956.07	1002.48
Lower Web	567.76	700.70	781.21	840.07
Rebar (Area)	63.48	127.24	198.52	272.64
Upper Web	146.73	229.10	295.46	354.08
Upper Flange	505.76	675.36	786.65	865.39
Concrete	15.78	30.74	52.13	73.79

After the nodal temperatures were obtained, the Equation 3.4 with the reduction coefficients for both the steel reinforcement and the steel deck, as well as for the concrete. These coefficients were extracted from prEN 1992-1-2 for the concrete and reinforcement, and from prEN 1993-1-2 for the steel deck. Figure 3.26 illustrates the reduction of the maximum moment capacity during the evolution of temperature in the elements that provide structural resistance.

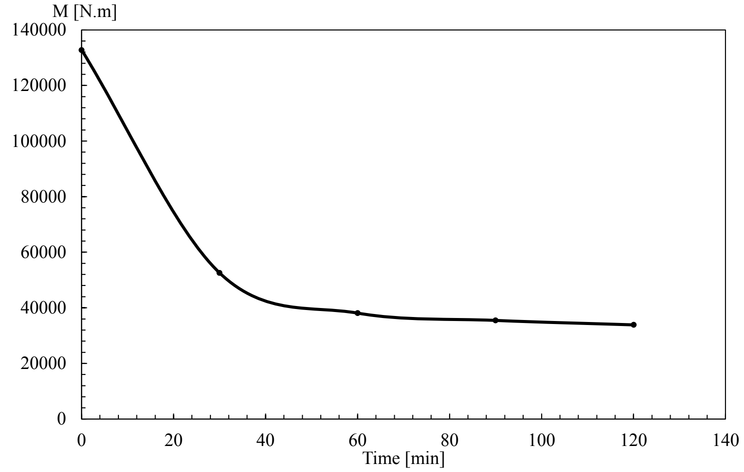

Figure 3.26: Evolution of moment capacity

3.3.3 Load application method in the numerical model

For the thermo-structural analysis, a constant load was applied over a period of time during which the slab temperature varied according to the thermal simulation results, using LS files to call these temperatures. In total, 720 LS files were inserted into the model, causing the temperature to increase every 10 seconds, aiming for better accuracy in the model. The final time was set at 7200 seconds with a maximum increment of 10 seconds and a minimum of 1×10^{-3}.

3.4 Performance criteria

As outlined in EN 1363:2020 [36], to qualify as structurally safe in the context of fire, an element must retain its load-bearing capacity, integrity, and insulation.

3.4.1 Loadbearing capacity

The load-bearing capacity is defined as the maximum load or weight a structure can support without undergoing failure or excessive deformations. This capacity is influenced by factors such as the thickness of slabs and environmental considerations, including exposure to fire. The Equations 3.6 and 3.7, defined in EN 1363:2020 [36], establish the limits for the element where L is the clear span of the test specimen, in millimeters and d is the distance from the extreme fiber of the cold design compression zone to the extreme fiber of the cold design tension zone of the structural section, in millimeters. The limiting deflection represents the maximum allowable vertical displacement of the slab, measured in millimeters. Simultaneously, the rate of deflection limit signifies the permissible rate of vertical displacement for the slab.

$$D_{limit} = \frac{L^2}{400 \times d}\,[mm] \tag{3.6}$$

$$\left(\frac{dD}{dt}\right)_{limit} = \frac{L^2}{9000 \times d}\,[mm] \tag{3.7}$$

The loadbearing failure occurs when the measured deflection is bigger than $1.5 \times D_{limit}$ or D_{limit} and $(dD/dt)_{limit}$ are exceeded. In the case of the slab studied, the value for D_{limit} is 242 mm and $(dD/dt)_{limit}$ is 10.8 mm/s.

3.4.2 Integrity

This criterion is deemed fulfilled when hot gases and flames stemming from the fire on one side of the element are effectively prevented from passing through the slab, thereby safeguarding the other side of the element.

3.4.3 Insulation

Regarding insulation, which is the capacity to prevent heat transfer from the exposed to the unexposed side. It is assumed that the criterion is met when the average temperature of the unexposed slab does not increase by more than 140 Kelvin, or the maximum temperature of the unexposed face does not exceed 180 Kelvin, both above the initial average temperature.

3.5 Advanced calculation method

In the construction industry, there is a constant pursuit of more economical means of building structures, and this also has an impact on the research field, as full-scale tests of buildings and elements, for example, require a considerable amount of financial resources. Considering this, techniques to replace or reduce these full-scale tests have emerged. Such techniques should be previously validated by experimental tests, eliminating the need for a series of samples to prove a particular result. One of the approaches to solving these problems, which is used in this thesis, is the Finite Element Method.

The finite element method (FEM) emerged as an approximation technique for solving problems in elasticity theory. This methodology is rooted in the variational principles of Rayleigh-Ritz and the weighted residual methods, particularly the Galerkin method.

The FEM prescribes a subdivision of a continuous domain of integration into small regions, referred to as finite elements. In this procedure, the continuous domain is treated as a discrete domain.

In a finite element mesh, each point of intersection is termed a 'node'. Consequently, each finite element is comprised of a set of nodes situated at its boundaries. Thus, this method involves determining the nodal variables. These variables depend on the physical characteristics of the continuum. For thermal problems, where the continuum is subjected to temperature variation, the variable to determine is the temperature. In mechanical problems, the nodal solutions consist of displacements.

The numerical modeling consists of defining an approximation function that describes the behavior of the structure. On the FEM, the functions are defined on the domain of the finite element, which implies that the function of potential energy Π_i is defined for each finite element and, when summed, they form the functional of the total potential energy Π for the entire discrete domain. This idea is formulated in Equation 3.8.

$$\Pi = \sum_{i=1}^{n} \Pi_i \tag{3.8}$$

The finite element is described by approximation functions, denoted as u_i, which are formed by multiplying shape or interpolating functions, denoted as N_i, with node variables, denoted as a_i. Typically, the shape functions are polynomials. This allows the shape functions to be defined by an Equation similar to (3.9) that describes their behavior.

$$\begin{aligned} u = \frac{1}{8}(&u_I(1-s)(1-t)(1-r) + u_J(1+s)(1-t)(1-r) \\ &+u_K(1+s)(1+t)(1-r) + u_L(1-s)(1+t)(1-r) \\ &+u_M(1-s)(1-t)(1+r) + u_N(1+s)(1-t)(1+r) \\ &+u_O(1+s)(1+t)(1+r) + u_P(1-s)(1+t)(1+r)) \end{aligned} \tag{3.9}$$

The shape function depicted above represents the displacement u of a hexaedric solid finite element, formulated with linear shape functions on s, t, and r (local coordinate system) along with the nodal displacements values u_j through u_p. Variational calculus is employed to characterize the potential energy functions, as shown in Equation 3.10

$$\Pi = \frac{1}{2}\int_V \varepsilon^T \sigma dV - \int_V u^T b dV \int_A u^T p dA \tag{3.10}$$

The first term corresponds to the internal strain energy, equal to the principle of virtual work performed by internal forces. The second and third terms correspond to the virtual work performed by the body force b and the external force p.

In representing the continuous system through energy functions, the equilibrium conditions, also referred to as stationarity, are determined by minimizing this function, which entails setting its first derivative to zero, as depicted in Equation 3.11.

$$\delta\Pi = \frac{1}{2}\int_V \varepsilon^T \sigma dV - \int_V u^T b dV \int_A u^T p dA = 0 \tag{3.11}$$

In problems of elasticity, the field of deformations and stresses is related through the constitutive relationship within the framework of virtual work. The 3D Hooke's law applies in the linear regime, as represented in Equation 3.12.

$$\begin{Bmatrix} \sigma_{xx} \\ \sigma_{yy} \\ \sigma_{zz} \\ \tau_{xy} \\ \tau_{xz} \\ \tau_{yz} \end{Bmatrix} = \frac{E}{(1+v)(1-2v)} \begin{bmatrix} 1-v & v & v & 0 & 0 & 0 \\ v & 1-v & v & 0 & 0 & 0 \\ v & v & 1-v & 0 & 0 & 0 \\ 0 & 0 & 0 & \frac{1-2v}{2} & 0 & 0 \\ 0 & 0 & 0 & 0 & \frac{1-2v}{2} & 0 \\ 0 & 0 & 0 & 0 & 0 & \frac{1-2v}{2} \end{bmatrix} \begin{Bmatrix} \epsilon_{xx} \\ \epsilon_{yy} \\ \epsilon_{zz} \\ \gamma_{xy} \\ \gamma_{xz} \\ \gamma_{yz} \end{Bmatrix} \tag{3.12}$$

The strains are written as a function of nodal displacements, through compatibility conditions, described in Equation 3.13

$$\begin{Bmatrix} \sigma_{xx} \\ \sigma_{yy} \\ \sigma_{zz} \\ \tau_{xy} \\ \tau_{xz} \\ \tau_{yz} \end{Bmatrix} = \begin{bmatrix} \frac{\partial}{\partial x} & 0 & 0 \\ 0 & \frac{\partial}{\partial y} & 0 \\ 0 & 0 & \frac{\partial}{\partial z} \\ \frac{\partial}{\partial y} & \frac{\partial}{\partial x} & 0 \\ 0 & \frac{\partial}{\partial z} & \frac{\partial}{\partial y} \\ \frac{\partial}{\partial z} & 0 & \frac{\partial}{\partial x} \end{bmatrix} \times \begin{Bmatrix} u \\ v \\ w \end{Bmatrix} \tag{3.13}$$

The solution to the energy minimization problem results in the equation $k_i \times u_i = f_i$ for each finite element, which, when summed over the entire domain, yields the global system of equations, represented in Equation 3.14

$$[K] \times \{u\} = \{F\} \tag{3.14}$$

Where K represents the stiffness matrix of the model, which is the sum of the stiffness matrix of each finite element and u denotes the vector of nodal displacements.

In thermal analysis, as in the present dissertation, the Finite Element Method (FEM) equations are established by the thermal capacity matrix combined with the heat exchange constants, multiplied by the vector of nodal parameters, which, in this case, represent the nodal temperatures. On the other side of the equation, the thermal action applied is represented.

The methodology applied to this study was divided into two parts, these being, thermal and mechanical simulations using different types of materials models, to represent each element more appropriately. Each simulation has its boundary conditions and is explained in the following items.

3.5.1 Newton-Raphson method

In numerous elasticity problems, it is imperative to precisely define the physical properties of materials, such as the modulus of elasticity, as a function of the stress and strain fields they manifest. This becomes essential when the applied load surpasses a threshold, leading to stress-strain ratios that extend beyond the linear elastic regime.

In these cases, it is necessary to use an incremental-iterative calculation method to solve nonlinear problems. Among several methods, such as the Secant method, Bisection method, and Arc Length method, the Newton-Raphson method is considered the most suitable for various nonlinear problems in solid mechanics.

In nonlinear problems, solved through incremental and iterative methods, the solution to the equation expressed in Equation 3.14 for determining the parameters u is now expressed as demonstrated in Equation 3.15.

$$\Psi_{n+1} = \Psi(a_n + 1) = f_{n+1} - P(a_n + 1) = 0 \tag{3.15}$$

Where F is the external force vector and P is the internal force which depends on the parameter u, which is associated with the stiffness matrix and the vector nodal parameter u, and the function Ψ_{n+1} is the function which represents the difference between internal and external forces. The function Ψ_{n+1} can be written in the form of Equation 3.16 on the incremental and iterative method.

$$\Psi(u_{n+1}^{i+1}) \simeq \Psi(u_{n+1}^{i}) + \left(\frac{d\Psi}{du}\right)_{n+1}^{i} du_n^i = 0 \tag{3.16}$$

On the the Equation 3.16 indicates that the value of the function Ψ on the iteration $i+1$ assumes the previous value summed with the increment $\left(\frac{d\Psi}{du}\right)_{n+1}^{i} du_n^i$. The force values of F and u are represented similarly as showed in Equations 3.17 and 3.18

$$F_{n+1} = F_n + \Delta F_n \tag{3.17}$$

$$u_{n+1} = u_n + \Delta u_n \tag{3.18}$$

Advancing in the discretization of the formulation, the Equation 3.19 is obtained.

$$P(u_{n+1}) = [K] \times u_{n+1} \tag{3.19}$$

Where the partial derivation of P generates the Equation 3.20

$$\partial P(u_{n+1}) = [K] \times \partial u_{n+1} \tag{3.20}$$

Considering the force vector F independent of displacement u, its derivative obtained from Equation 3.20 results in Equation 3.21.

$$\partial \Psi = -\partial P = -K_T \times \partial u = 0 \rightarrow K_T = \frac{\partial \Psi}{\partial u} \tag{3.21}$$

Substituting $[K]$ from Equation 3.21 into 3.16 yields Equation 3.22.

$$K_T^i \times du_n^i = \Psi_{n+1}^i \tag{3.22}$$

Isolating the variable parameter du, is obtained Equation 3.23

$$du_n^i = \left(K_T^i\right)^{-1} \times \Psi_{n+1}^i \tag{3.23}$$

In a series of successive approximations, the unknown parameter u_{n+1}^{i+1} is the sum of the value at the previous step and the increment du_{n+1}^{i}, resulting in Equation 3.24.

$$u_{n+1}^{i+1} = u_{n+1}^{i} + du_{n+1}^{i} \tag{3.24}$$

The unknown parameter can be represented as the initial value plus the sum of successive increments, resulting in Equation 3.25

$$u_{n+1}^{i+1} = u_n + \sum_{k=1}^{i} du_n^k \tag{3.25}$$

Chapter 4

Results

In this section, the results obtained from the thermal and mechanical simulations will be presented, along with the analysis and comparison of the data obtained concerning the experimental data.

4.1 Thermal simulation

The results obtained in the ANSYS software were compared with those obtained in the laboratory test provided by the reference. For the accuracy of the comparison, nodes with positions equal to or similar to those of the thermocouples used and reported in the experimental test were selected. Temperatures recorded in the finite element software SAFIR were also compared, and extracted from the test report [26]. The root mean square error (RMSE), which is a performance indicator for a regression model, aimed at measuring the average difference between two data sets—in this thesis, the experimental model and the numerical model (ANSYS). RMSE is governed by Equation 4.1. The locations of the 10 analyzed points are illustrated in Figure 4.1 below.

$$RMSE = \sqrt{\sum_{i=1}^{n} \frac{(\hat{y}_i - y_i)^2}{n}} \tag{4.1}$$

Where n is the number of samples, $\hat{y}_i$ is the observed value and y_i is the predicted value.

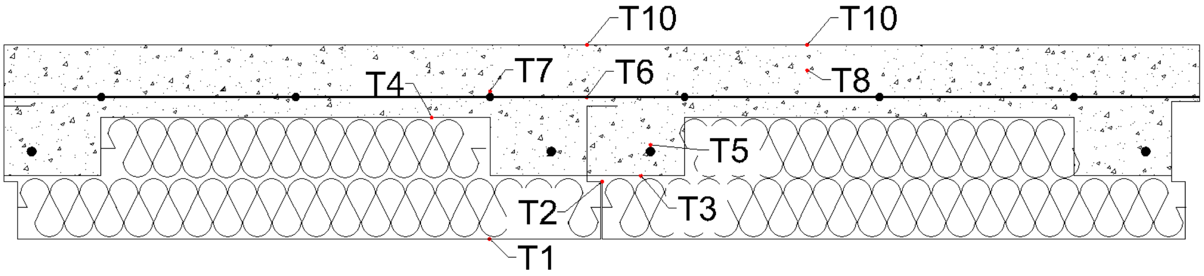

Figure 4.1: Location of thermocouples

Point T1, located at the base of the steel deck and exposed to fire, exhibited an RMSE of 66.16 °C, closely approximating the laboratory-recorded temperature. Considering that temperatures on the deck can peak at around 950 °C, this discrepancy is acceptable and also, according to EN 1363-1 [36], at any time after the first 10 minutes of the test, the temperature recorded by the any thermocouple in the furnace shall not differ from the corresponding temperature of the standard temperature/time curve by more than 100 °C. Conversely, Point T2, positioned in the gap between sheet junctions, recorded an RMSE of 132.55 °C, slightly higher than expected. Nevertheless, both the numeric results from ANSYS and those from SAFIR, provided by the document [26], observed in Figure 4.2 (a), demonstrate that the numerical strategy presented in this dissertation results in satisfactory results.

Points T3 and T4, in Figure 4.2 (b), located at the concrete and mineral wool interface but at different heights, showed RMSE errors of 30.26 °C and 24.21 °C, respectively. Point T3, the nearest point to T2, did not suffer from the influence of the imprecision of the thermal field at T2. This shows that, in uniform areas, regarding the discretization of the continuous domain, the numerical strategy yields accurate results. Similarly, Point T5, in the reinforcement region, yielded an RMSE of 94.86 °C, maintaining a difference of less than 100 °C from the experimental test due to the varying heat absorption of metal and concrete elements. Points T6 and T7, near the steel mesh, had RMSE values of 40.20 °C and 36.95 °C, respectively. Additionally, Point T8, in the middle of the concrete above the mineral wool, had an RMSE of 16.51 °C. Finally, points T9 and T10, in figure 4.2(e), on the unexposed faces, recorded RMSE values of 5.56 °C and 12.5 °C, indicating close agreement between the ANSYS software and the test described in the utilized report. These results are illustrated in Figure 4.2.

The numerical simulation conducted in the software and the experimental results from the reference [26] met the insulation and integrity criteria required by EN 1363-1 (2020) [36]. The maximum temperature on the unexposed face did not exceed 180 Kelvin at any point and did not experience an average temperature rise of more than 140 Kelvin above the initial temperature. The test also met the integrity criterion, as no gas penetration was observed during the experiment, and the temperatures recorded in the software were insufficient to ignite the cotton.

Figure 4.2 also illustrates the values extracted from the report for the SAFIR software, which was used to validate the experimental results [26]. ANSYS achieves greater accuracy in results compared to SAFIR. Table 4.1 shows the temperature difference calculated with Root Mean Square Error

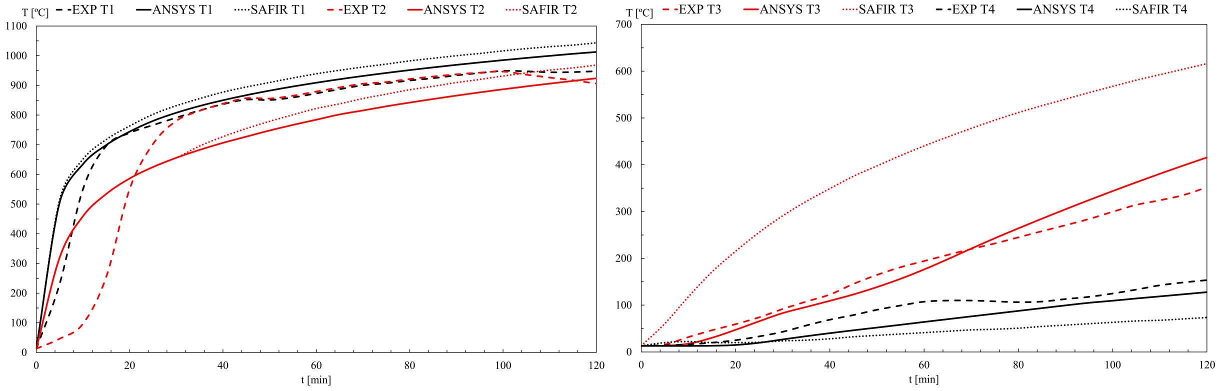

a) T1 and T2 **b) T3 and T4**

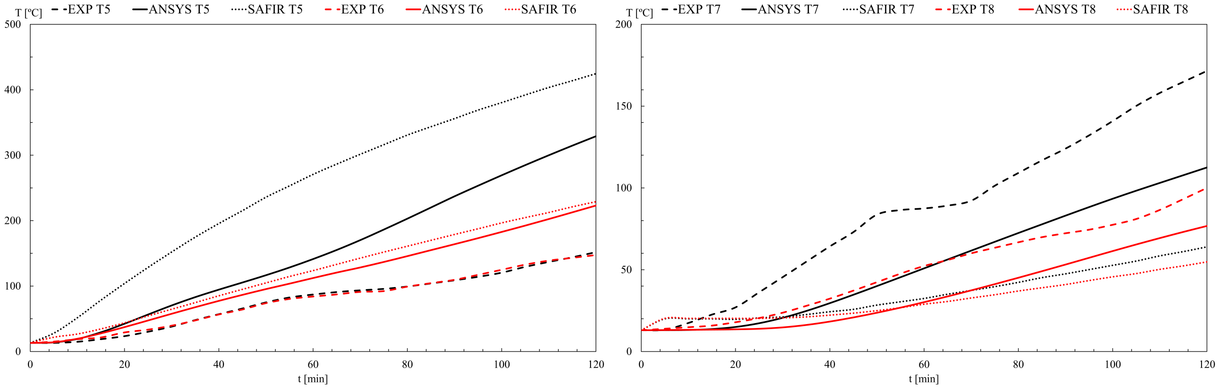

c) T5 and T6 **d) T7 and T8**

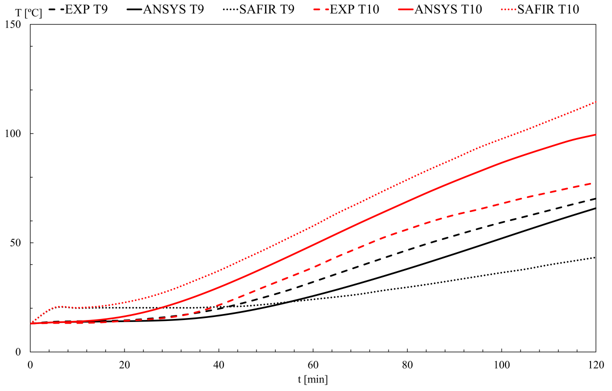

e) T9 and T10

Figure 4.2: Results Thermal Simulation

Table 4.1: Root Mean Square Error

POINT	**LOCATION**	**RMSE**
T1	Base of Steel Deck	66.16
T2	Gap between the decks	132.55
T3	Concrete and Mineral Wool Interface	30.26
T4	Concrete and Mineral Wool Interface	24.21
T5	Reinforcement	94.86
T6	Steel mesh	40.20
T7	Steel mesh	36.95
T8	Concrete	16.51
T9	Unexposed face	5.56
T10	Unexposed face	12.50

Figures 4.3, 4.4, 4.5 and 4.6 displays the temperature field at the end of 30 minutes, 60 minutes, 90 minutes and 120 minutes of the simulation in the middle of the span, revealing all structure elements. The significant influence of the gap between the steel decks on heat dissipation in the structure is evident.

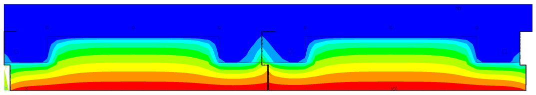

Figure 4.3: Thermal field at 1800 s

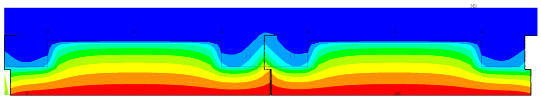

Figure 4.4: Thermal field at 3600 s

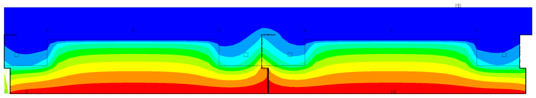

Figure 4.5: Thermal field at 5400 s

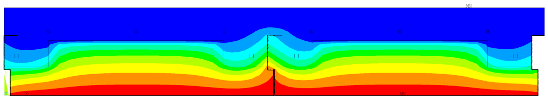

Figure 4.6: Thermal Field at 7200 s

Figure 4.7 shown the temperature field in the 3D model at the end of 7200 seconds.

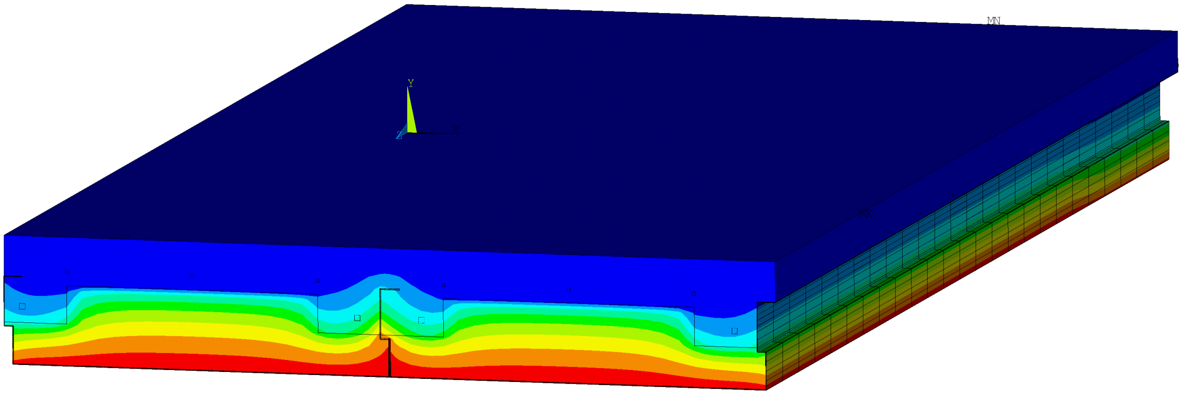

Figure 4.7: Slab on 3D perspective at 7200 s

4.2 Mechanical Simulation

At ambient temperature, according to the simplified calculation methods in the analytical solution, it was expected that with a total force of 120,687.20 N divided among 276 nodes, all of which are located at the load application interface, totaling 874.54 N per node, the slab would reach its load resistance limit. In numerical moment terms, this force represents 132.75 $kN.m$.

With the incremental force solution method (GMNIA), the slab resisted up to a load of 857.50 N per node, achieving a resistance moment of 130.17 $kN.m$. These results showed a difference of 1.98%. The deformed slab is shown in Figure 4.8.

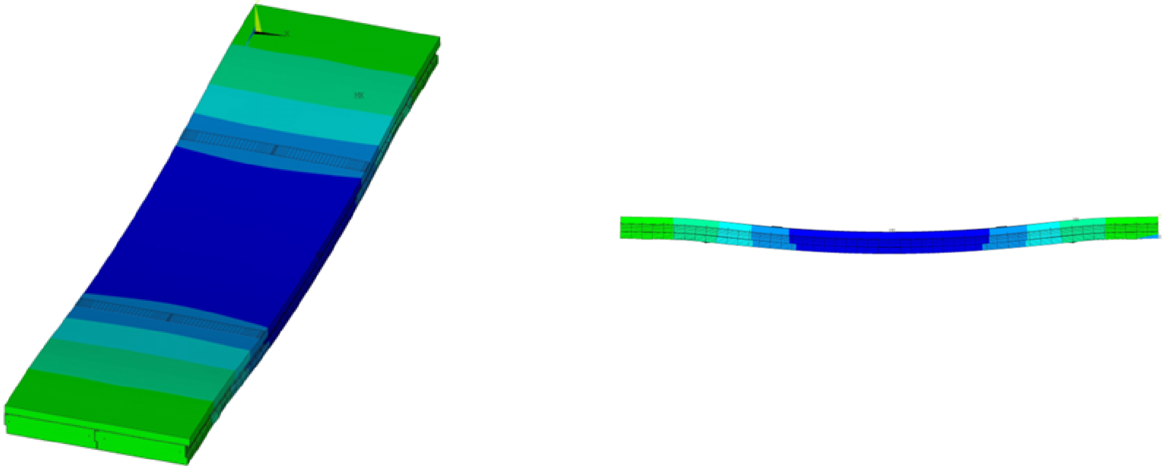

Figure 4.8: Deformed model at the end of the simulation

In the displaced form, showed by the curvature and colours illustrated in Figure 4.8, the steel deck and concrete are continuously connected, as assigned in the model, no friction loss was considered. Therefore, the structural model at ambient temperature exhibited the expected behavior.

The displacement in the vertical direction (Y) was measured during the evolution of the load in the numerical simulation. Figure 4.9 shows the displacement progression at a selected node in the middle of the span, where both the moment and displacement are maximum. The slab suffered a maximum displacement of 11.3 millimeters at the end of the simulation.

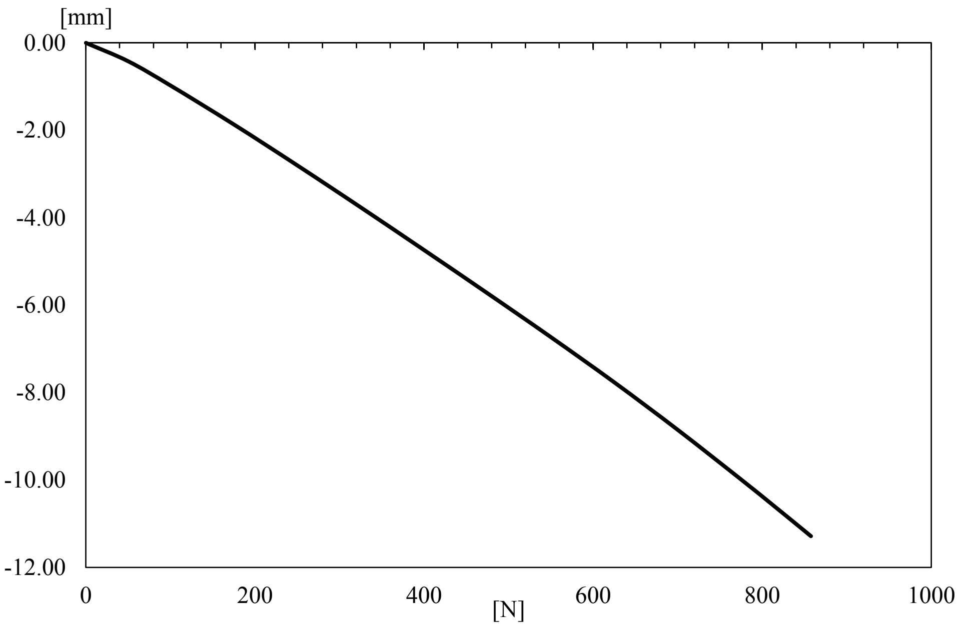

Figure 4.9: Displacement at the middle of the span

4.3 Thermo-mechanical procedure

4.3.1 Analytical method

The load-bearing capacity of the slab was obtained through the pr EN1994-1-2 [34], however, due to the complexity of the deck's geometry, the temperature fields present in the slab cannot be applied, as they are designed for a specific type of composite slab. The study of the temperature field calculated in the numerical model was important for the analytical resistance calculation.

4.3.2 Numerical method

The thermostructural model is processed in stages. The first stage consists of applying the force. Since this value is small, as it is a proportion of the maximum force, the numerical model remains stable, and convergence is achieved with few processing steps.

Consequently, the behavior of the slab regarding its stress and strain field is easily determined.

In the second stage and subsequent ones, the transient thermal field obtained from the thermal analysis is applied to the structural model in incremental intervals of 10 seconds, as described in 3.3.2. The mechanical properties of each structural material are altered according to their respective temperatures.

In the initial time increments, where the underside of the steel deck still has a temperature of up to 100 ℃, no reduction in yield and ultimate stresses, as well as in the modulus of elasticity, is recorded. On the other hand, this metallic material already exhibits thermal expansion in the middle of the span, where there is no contact between the steel sheet and the concrete. Since this span has its longitudinal displacement prevented at the ends, the expansion results in compression and instability behavior in the lower sheet.

The numerical solution for instability behavior would require analyzing more complex numerical strategies, including a new mesh study to determine the best refinement for models subjected to generalized states of stress and strain, modal analysis of elastic instability to alter the geometry of slender elements to consider their buckling modes and analysis of the contact interface between steel and concrete at the ends of the slab to determine relative displacement due to loss of frictional resistance.

Due to the complexity level of the thermostructural numerical model, which would require review and completion in a short period, the resistance criterion was verified based on the procedure prescribed in eurocode [10]. In this analysis, the thermal field was extracted from the thermal analysis of this study.

Chapter 5

Conclusions

5.1 Thermal analysis

The study presented the development of a thermal simulation conducted with finite elements that validated an experimental test extracted from a reference article. According to pr EN1994-1-2, the insulation criterion, which requires that the increase in average temperature on the unexposed side does not exceed 140 Kelvin above the initial average temperature, was met, as points T9 and T10 reached maximum temperatures of 65.79 °C and 99.50 °C, respectively. Also, the criterion that requires that any point of the nonexposed face does not reach temperatures higher than 180 Kelvin was achieved.

It is noticeable that the result obtained by the software differs from the experimental one at the beginning of the test (5 to 15 minutes) and over time. It was observed that the view factor of the 2 mm opening was an important parameter for the simulation temperature to be close to the experimental temperature in this region. The thermal model can be used for parametric studies using material properties and correct simulation parameters.

5.2 Mechanical analysis

Given that the slab has a high level of complexity in its geometry and there is no specific procedure to calculate the maximum moment resistance in the standards, achieving a difference of 1.98 % between the simulation and the analytical calculation can be considered a high precision simulation test. The so-called sharp corners where the concrete, steel deck and mineral wool materials meet create an instability phenomenon in the software, which can hinder convergence with more accurate results.

5.3 Thermo-mechanical conclusion

On the numerical simulation, once the boundary conditions were applied for displacement, and ANSYS still applies the default conditions for moment and force, the steel deck expands due to the temperature increase of the slab and the thermal expansion properties of steel, experiencing thermal compression because of the support conditions applied at its end. As a result, the Newton-Raphson method fails to converge with the rising temperatures.

Although the calculation was performed analytically following the standard, the numerical thermal simulation was crucial for obtaining the components' temperatures throughout the temperature rise. This is because, for this type of slab, the standard does not establish a temperature field to be used for the application of reduction coefficients.

5.4 General conclusion

The results of both thermal and mechanical simulations have shown that finite element software is capable of analyzing structures in both fields. However, the accuracy of the analysis depends on the correct input of physical properties and proper modeling of the structure. These two factors are fundamental for accurate results to be obtained.

5.5 Future works

For the future works is recommended the list below.

- Perform a new mesh study and continue with the thermo-structural modeling.
- Inserting a concrete fracture model, in the case of ANSYS, the Solid65 element is the most recommended.
- Perform thermo-structural simulation using the temperature field, considering the instability modules of the steel, as it is subject to thermal compression.
- Conduct a new experimental study using different span measurements.
- Increase the span of the numerical study.

Bibliography

[1] R. Johnson, *Composite Structures of Steel and Concrete*, Third Edit. Blackwell Publishing, Sep. 2004, p. 230, ISBN: 9781405100359. DOI: `10.1002/9780470774625`. [Online]. Available: `https://onlinelibrary.wiley.com/doi/book/10.1002/9780470774625`.

[2] J. W. Rackham, G. H. Couchman, and S. J. Hicks, *Composite slabs and beams using steel decking: Best practice for design and construction.* Metal Cladding amp; Roofing Manufacturers Association in partnership with the Steel Construction Institute, 2009.

[3] G. M. E. Cooke, R. M. Lawson, and G. M. Newman, "Fire resistance of composite deck slabs," *The Structural Engineer*, pp. 253–267, 1988.

[4] I. M. Ahmed and K. D. Tsavdaridis, "The evolution of composite flooring systems: Applications, testing, modelling and eurocode design approaches," *Journal of Constructional Steel Research*, vol. 155, pp. 286–300, 2019, ISSN: 0143-974X. DOI: `https://doi.org/10.1016/j.jcsr.2019.01.007`. [Online]. Available: `https://www.sciencedirect.com/science/article/pii/S0143974X18307296`.

[5] R. M. Schuster, "Strength and behaviour of cold-rolled steel deck reinforced concrete floor slabs," Ph.D. dissertation, Iowa State University, Ames, Iowa, 1970.

[6] *Indoor Air*, vol. 18, no. 3, pp. 182–201, 2008. DOI: `https://doi.org/10.1111/j.1600-0668.2007.00516.x`. eprint: `https://onlinelibrary.wiley.com/`

`doi/pdf/10.1111/j.1600-0668.2007.00516.x`. [Online]. Available: `https://onlinelibrary.wiley.com/doi/abs/10.1111/j.1600-0668.2007.00516.x`.

[7] K. Mróz, I. Hager, and K. Korniejenko, "Material solutions for passive fire protection of buildings and structures and their performances testing," *Procedia Engineering*, vol. 151, pp. 284–291, 2016, Ecology and new building materials and products 2016, ISSN: 1877-7058. DOI: `https://doi.org/10.1016/j.proeng.2016.07.388`. [Online]. Available: `https://www.sciencedirect.com/science/article/pii/S1877705816317763`.

[8] Z. Panossian, L. Mariaca, M. Morcillo, *et al.*, "Steel cathodic protection afforded by zinc, aluminium and zinc/aluminium alloy coatings in the atmosphere," *Surface and Coatings Technology*, vol. 190, no. 2-3, pp. 244–248, 2005. DOI: `10.1016/j.surfcoat.2004.04.023`.

[9] ECCS, *Calculation of fire resistance of composite concrete slabs with profiled steel sheet exposed to the standard fire*, Rotterdam: ECCS - Technical Committee, 1983.

[10] CEN, European Committee for Standardization, *Eurocode 4 part 1.2: Design of composite steel and concrete structures - structural fire design*, Brussels, 1993.

[11] International Organization for Standardization, *ISO 834-11 - Fire resistance tests — Elements of building construction*, Geneva, 2014.

[12] R. Hamerlinck and L. Twilt, "Fire resistance of composite slabs," *Journal of Constructional Steel Research*, vol. 33, no. 1, pp. 71–85, 1995, Special Issue on Fire and Steel, ISSN: 0143-974X. DOI: `https://doi.org/10.1016/0143-974X(94)00015-A`. [Online]. Available: `https://www.sciencedirect.com/science/article/pii/0143974X9400015A`.

[13] R. Hamerlinck, "The behaviour of fire-exposed composite steel/concrete slabs," Ph.D. dissertation, Eindhoven University of Technology, 1991.

[14] CEN, *En 1994-1-2: Design of composite steel and concrete structures - structural fire design*, Brussels: European Committee of Standardization, 2004.

[15] K. Both, "Fire-exposed continuous span composite steel-concrete slabs," *HERON*, vol. 41, no. 3, 1996, TU Delft/TNO Bouw Centre for Fire Research, P.O. Box 49, 2600 AA Delft, ISSN: 0046-7316.

[16] C. G. Bailey, T. Lennon, and D. B. Moore, "Título do artigo (se disponível)," *The Structural Engineer*, vol. 77, no. 8, Apr. 1999.

[17] C. G. Bailey and D. B. Moore, "The structural behaviour of steel frames with composite floorslabs subjected to fire - part 1: Theory," *The Structural Engineer*, vol. 78, no. 11, pp. 19–27, 2000.

[18] A. H. Buchanan and A. K. Abu, *Structural Design for Fire Safety.* University of Canterbury, New Zealand: John Wiley & Sons, Ltd, 2017.

[19] P. A. G. Piloto and et al., "Three-dimensional numerical modelling of fire exposed composite slabs with steel deck," *MATTER: International Journal of Science and Technology*, vol. 5, no. 2, pp. 48–67, 2019.

[20] C. Balsa, L. Santos, P. A. G. Piloto, and É. Kimura, "Effect of the load level in the fire resistance of composite slab with steel decking," in *Congresso Ibero-Latino-Americano em Segurança contra Incêndio*, 15 Julho 2019.

[21] F. Bolina, B. Tutikian, and J. P. C. Rodrigues, "Thermal analysis of steel decking concrete slabs in case of fire," *Fire Safety Journal*, vol. 121, p. 103 295, 2021, ISSN: 0379-7112. DOI: `https://doi.org/10.1016/j.firesaf.2021.103295`. [Online]. Available: `https://www.sciencedirect.com/science/article/pii/S0379711221000229`.

[22] C. Balsa, M. B. Silveira, V. Mange, and P. A. G. Piloto, "Computational modeling of the thermal effects on composite slabs under fire conditions," in *Advanced Research in Technologies, Information, Innovation and Sustainability: Proceedings of the First International Conference, ARTIIS 2021*, La Libertad, Ecuador: Springer, Nov. 2021.

[23] F. L. Bolina and J. P. C. Rodrigues, "Finite element analysis criteria for composite steel decking concrete slabs subjected to fire," *Fire Safety Journal*, vol. 139, p. 103 818, 2023, ISSN: 0379-7112. DOI: `https://doi.org/10.1016/j.firesaf.2023.103818`. [Online]. Available: `https://www.sciencedirect.com/science/article/pii/S0379711223000863`.

[24] P. A. G. Piloto, C. Balsa, E. Kimura, and G. Lucca, "Comportamento ao fogo de lajes mistas com chapa de aço colaborante," in *1º Congresso Brasileiro de Estruturas Mistas (CBEM24)*, Universidade Estadual de Mariná, Maringá/PR, Brasil, Abril 15-17 2024.

[25] Y. Wang, Ed., *Steel and Composite Structures: Behaviour and Design for Fire Safety*, 1st. CRC Press, 2002, https://doi.org/10.1201/9781482267693.

[26] CSTB le futur en construction, *Étude du comportement au feu du plancher cofradal 200*, ARCELOR Construction France, 5 rue Gaston Planté, 34790 GRABELS.

[27] Y. A. Cengel and A. J. Ghajar, *Heat and mass transfer: fundamentals and applications*, Fitfh Edit. New York: McGraw-Hill Education, 2014, p. 991, ISBN: 0077654765.

[28] J. B. J. Fourier, *Théorie Analytique de la Chaleur* (Cambridge Library Collection - Mathematics). Cambridge University Press, 2009. DOI: `10.1017/CBO9780511693229`.

[29] J. H. Lienhard IV and J. H. Lienhard V, *A Heat Transfer Textbook*, 5th. Cambridge, MA: Phlogiston Press, Aug. 2020, 784 pp., Version 5.10. [Online]. Available: `http://ahtt.mit.edu`.

[30] CEN, European Committee for Standardization, *Pr en 1993-1-2 - eurocode 3 - design of steel structures - part 1-2: Structural fire design*, Brussels, Oct. 2023.

[31] CEN, European Committee for Standardization, *Pr en 1992-1-2 - eurocode 2: Design of concrete structures - part 1-2: General rules - structural fire design*, Brussels, Sep. 2021.

[32] CEN, European Committee for Standardization, *Pr en 1995-1-2 - eurocode 5 – design of timber structures*, Brussels, Dec. 2022.

[33] European Committee for Standardization, *Eurocode 1: Actions on structures - part 1-2: General actions - actions on structures exposed to fire*, English, Supersedes ENV 1991-2-2:1995, Nov. 2002. [Online]. Available: `https://doi.org/10.3403/00071057`.

[34] CEN/TC 250, *Eurocode 4 — design of composite steel and concrete structures — part 1-2: Structural fire design*, Secretariat: BSI, European Committee for Standardization, Dec. 2022.

[35] L.-G. Cajot, "Fire resistance assessment of composite structures: Basic design methods, worked examples," in *Workshop 'Structural Fire Design of Buildings according to the Eurocodes'*, Chairman of CEN/TC250/SC4/EG - Fire Part, CEN/TC250/SC4/EG - Fire Part, ArcelorMittal, Brussels, Nov. 2012.

[36] European Committee for Standardization, *En 1363-1: Fire resistance tests - part 1: General requirements*, ICS 13.220.40; 13.220.50, Ref. No. EN 1363-1:2020 E, Feb. 2020.